Journal of Environmental Management 384 (2025) 125542

Contents lists available at ScienceDirect

Journal of Environmental Management

journal homepage: www.elsevier.com/locate/jenvman

Research article

Improved integrated framework for flooded crop damage and recovery assessment: A multi-source earth observation and participatory mapping in Hadejia, Nigeria

Lukumon Olaitan Lateef [a,*], Hugo Costa [a,b], Pedro Cabral [c,a,**]

[a] NOVA Information Management School (NOVA IMS), Universidade NOVA de Lisboa, Campus de Campolide, 1070-312, Lisboa, Portugal
[b] Direção-Geral do Território, Rua Artilharia Um, 107, 1099-052, Lisboa, Portugal
[c] School of Remote Sensing and Geomatics Engineering, Nanjing University of Information Science & Technology, Nanjing, 210044, China

ARTICLE INFO

Handling Editor: Dr. Lixiao Zhang

Keywords:
Flood
Crop recovery
Damage assessment
Earth observation
Machine learning
Participatory mapping

ABSTRACT

Flooding has increasingly significant adverse effects on global food security, and there is a lack of a framework to effectively integrate remote sensing with survey data for accurate damage and recovery assessment. Also, optical satellite images for flood mapping face cloud interference, and free synthetic aperture radar (SAR) lack the temporal frequency needed to capture flooding dynamics. This study developed a new framework for modelling crop damage, loss, and recovery due to flash flooding using time-series multi-sensor satellite images. Crop recovery from remote sensing was validated with extensive participatory mapping data. Crop damage and recovery were assessed during Nigeria's 2020 and 2022 floods. Consistency was found between farmer-reported losses and remote sensing-based damage assessments: 91 % of farmers reporting total crop loss had no recovery. Flood maps and crop recovery assessments achieved over 90 % accuracy, demonstrating the reliability of multi-source optical and SAR satellite images combined with a machine learning technique. Severe flood damage was evident, with only 13 % and 16 % of flooded cropland recovered in 2020 and 2022, respectively. The integrated approach developed in this study eliminates uncertainties in other remote sensing techniques, overcomes participatory mapping limitations, and offers scalability for national-level implementation, providing critical information for post-disaster planning, farmer compensation, and sustainable agricultural practices to enhance food security in a changing climate.

1. Introduction

Floods are recurring global disasters, and the unprecedented weather events arising from climate change and anthropogenic factors are causing increasing cases of flooding (Thomas and López, 2015). This is leading to the devastating loss of lives and properties and severe damage to agricultural productions (Intergovernmental Panel on Climate Change (IPCC), 2023). The rapidly growing population is driving the expansion of croplands due to the high demand for food (Thenkabail et al., 2021). However, continuous rainfall-induced flooding remains one of the greatest threats to food security globally (Reed et al., 2022). This is because of its climate-dependence nature and the location of agricultural lands in floodplains, which are highly susceptible to flooding (Brémond et al., 2013). Flood water disrupts crop growth by altering the physiological functions necessary for sustaining crop health and yield (Zhou et al., 2020). According to the Sendai Framework Monitor, floods contribute mainly to annual agricultural losses from disasters; 16 percent of these losses, approximately USD 2.08 billion per year on average (Food and Agriculture Organization (FAO), 2023a). A large expanse of cropland is being destroyed by floods yearly, causing low yields, worsening the food security condition, having severe impacts on the livelihood of farmers (Chiaka et al., 2022; Food and Agriculture Organization (FAO), 2023b). This serves as a significant setback for countries in achieving the Sustainable Development Goal (SDG) 2 of zero hunger before the 2030 deadline (Echendu, 2022; Food and Agriculture Organization (FAO), 2023a). Agricultural disaster risk reduction and climate adaptation strategies require accurate information on the impacts of disasters on agriculture and economic loss. However, this is

* Corresponding author. NOVA Information Management School (NOVA IMS), Universidade NOVA de Lisboa, Campus de Campolide, 1070-312 Lisboa, Portugal.
** Corresponding author. School of Remote Sensing and Geomatics Engineering, Nanjing University of Information Science & Technology, Nanjing, 210044, China.
E-mail addresses: 20221058@novaims.unl.pt, lateeflukumon8@gmail.com (L.O. Lateef), cabral@nuist.edu.cn (P. Cabral).

https://doi.org/10.1016/j.jenvman.2025.125542
Received 1 October 2024; Received in revised form 13 April 2025; Accepted 24 April 2025
Available online 30 April 2025

being impeded by inconsistency in existing information and a lack of comprehensive approach to agricultural loss from flood disaster (Food and Agriculture Organization (FAO), 2023a).

The damage assessment methods for flood-affected crops include a survey and statistical approach, geospatial and remote sensing techniques, and hydraulic modeling. The survey-based approach has been used extensively by scientists (Amaechina et al., 2022; Idoko, 2016) and international organizations such as the United Nations Development Programme (UNDP) and Food and Agriculture Organization (FAO) (Food and Agriculture Organization (FAO), 2023a; United Nations Development Programme (UNDP), 2023). This involves conducting household surveys using structured questionnaires to obtain data from the targeted sample populations (farmers) and the statistical analysis of this data to infer damage and loss. This method is time-consuming and labour-intensive (H. Chen et al., 2019), and the dependent nature of the sampling approach introduces bias in the generalization of the results (Rahman and Di, 2020). Other limitations of this approach include a lack of information on the spatio-temporal dynamics of floods (X. Wang et al., 2022b), the subjectivity based on the ability of the respondents to recall the events, uncertainty regarding whether respondents have their farms within the study area, as most surveys are not conducted on the farms themselves, and geographic coordinates are not recorded. This calls for an efficient approach to flooded crop damage assessment (Reed et al., 2022). Another approach is hydraulic modelling with expert-based knowledge and household surveys for regression analysis to estimate yield loss and cropland damage (Monteleone et al., 2023; Shrestha et al., 2021). In existing studies, this method uses flood depths and durations from household surveys and relies on assumptions on damageable flood depth and crop height, which introduce biases (Monteleone et al., 2023).

Remote sensing images are instrumental in rapidly evaluating crop development and accurately quantifying flood-induced crop damage, loss, and recovery (Chen et al., 2019; Rahman and Di, 2020). The assessment of impacts and damages of floods to crops requires a reliable flood extent layer to ensure an accurate estimation of the affected crop areas and subsequent calculation of damage and loss (Bofana et al., 2022). Also, flood progression layers are crucial to show the dynamics of flash floods and are essential for modeling the recovery status of crops after flood events. The two types of satellite images are commonly employed for flood mapping: Optical and Synthetic Aperture Radar (SAR). Optical sensors depend on sun illumination, which limits their ability to capture clear images of the Earth's surface when there are high clouds or at night. SAR satellite imagery has proven indispensable for flooding mapping, primarily due to its cloud-penetrating capability and solar illumination independence (Clement et al., 2018; Demissie et al., 2023).

The most common approaches to detecting and delineating flooded extents from satellite images are Change Detection and Thresholding (CDAT) (Clement et al., 2018; Long et al., 2014), histogram thresholding, and multi-scale segmentation (Martinis et al., 2009), Global Otsu Thresholding (Otsu, 1979), region growing (Matgen et al., 2011), Normalized Difference Flood Index (NDFI) (Cian et al., 2018), Modified Normalized Difference Water Index (MNDWI) (Xu, 2006), active contour model, DEM filling, supervised classification using machine learning (Tong et al., 2018; Zhang et al., 2021) and deep learning approaches (Jamali et al., 2024; Saleh et al., 2024; Zhao et al., 2023). The concept of thresholding is categorizing areas exhibiting values lower than a designated threshold as flooded areas. Images with pixels that have bimodal distribution are suitable for the Otsu thresholding (Chen and Zhao, 2022). CDAT involves the arithmetic difference of the pre-flood (reference) image from the flooded image and subsequent extraction of the flooded areas from the difference image using a threshold (Long et al., 2014). NDFI, designed for Sentinel-1 (S-1) data, is a fast approach for flood mapping, which requires a substantial amount of reference images and is most suitable for multi-temporal images. A summary of the most common and widely used methods of flood mapping is discussed in Cian et al. (2018). MNDWI and similar water indices are applicable for flood extent extraction from optical satellite images. Methods such as NDFI, backscatter thresholding, and interferometric coherence are specific to SAR images. CDAT, ML, DL, histogram thresholding, region growing, and multi-scale segmentation techniques can be applied to both optical and SAR images.

Remote sensing–based flooded crop damage assessments from previous studies have employed the aforementioned flood mapping approaches combined with other geospatial analyses, such as the overlay of the flood layer and the cropland layer, to determine the extent of flooded cropland (Kumar et al., 2022; Pandey et al., 2022; Singha et al., 2020; L.-C. Wang et al., 2022a). Studies that assessed the degree of crop damage and recovery patterns have used Normalized Difference Vegetation Index (NDVI) differences from multi-temporal images (Bofana et al., 2022; Cui et al., 2023; Pantaleoni et al., 2007; Qamer et al., 2023), supervised classification (M. Li et al., 2022b), or used ground truth sample data and pictures of flooded cropland with NDVI ratios (Miao et al., 2023).

The NDVI approach is fast processing, but the result is limited by a lack of sufficient data on the effect of inter/intra annual climatic and phenological variability of crops (Wang et al., 2020), and threshold selection introduces subjectivity. Some studies (Dodangeh and Shah-Hosseini, 2023; Kumar et al., 2022; M. Li et al., 2022b; Singha et al., 2020) used the CDAT for flood mapping, which has been found to under/overestimate flooding extent (C. Li et al., 2022a). While the S-1 imagery overcomes clouds during floods, the revisit period/temporal resolution of 6–12 days is not suitable for capturing flash flood dynamics (Demissie et al., 2023). Furthermore, coarse-resolution land cover data (10–30m) used in previous studies could lead to inaccurate quantification of cropland extent (Kang et al., 2022). Lastly, remote sensing results on crop damage, loss, and recovery from existing studies lack sufficient ground validation, raising reliability concerns for decision-making (Rahman and Di, 2020; Reed et al., 2022). To improve the methods of flooded crop damage and recovery assessment, this study develops an integrated machine learning (ML) method using multiple satellite-derived indicators, including flood frequency and spectral indices and participatory mapping data. The effectiveness of multi-source satellite images for precise spatio-temporal flood mapping and assessing crop damage and recovery was evaluated. This research used high-resolution (3m) imagery for accurate land cover. The limitations of participatory mapping were addressed by using it as ground truth to validate satellite-based assessments. This study advances scientific methodologies by providing a reliable workflow for integrating remote sensing and participatory mapping for flooded crop damage assessment and recovery. This is valuable for accurate damage quantification and provides a valuable framework for policymakers in disaster response, such as the UNDP and FAO, who face challenges with inconsistent and delayed flood impact data on crop production (Food and Agriculture Organization (FAO), 2023a), especially as the United Nations (UN) launched a new fund to support countries that have suffered from flood and climate-induced disasters (United Nations Development Programme (UNDP), 2024).

2. Data and methods

2.1. Study region

In Africa, Nigeria has been one of the most affected countries by flooding over the last 20 years, which is caused by torrential rainfall, the release of water from dams, and unguided urbanization (Nigeria Hydrological Services Agency, 2022; Umar and Gray, 2023). The devastating 2022 floods in Nigeria left a profound impact, destroying more than 676,000 ha of farmland across 34 states and displacing more than two million people. This catastrophic event underscores the urgent need for adequate flooded crop damage assessment and recovery strategies (National Emergency Management Agency (NEMA), 2023; United

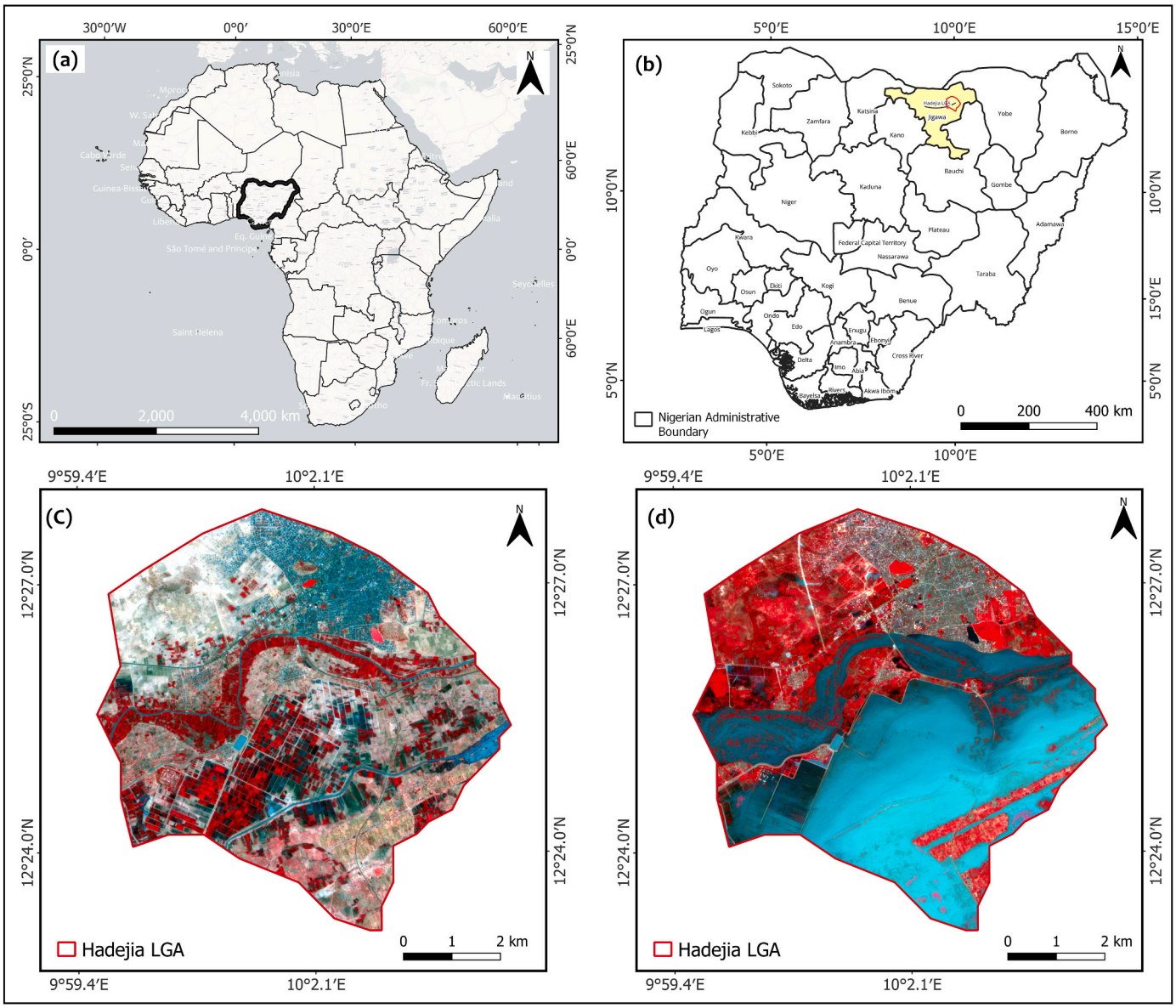

Fig. 1. Study location map showing (a) Africa, (b) Nigeria. PlanetScope False Colour Composite (FCC) image of the: (c) analysis extent during the farming season in July 2022, and (d) analysis extent during the flood in September 2022. (Satellite Image Source (Planet Labs, 2023a):). *Basemaps provided by CARTO (*https://carto.com/attribution*) and OpenStreetMap (*https://www.openstreetmap.org/copyright*). Map lines delineate study areas and do not necessarily depict accepted national boundaries.*

Nations Office for the Coordination of Humanitarian Affairs (OCHA), 2022). The agrarian region of Hadejia in Nigeria has been selected for this research based on the historical flooding incidences and predominant crop cultivation (Fig. 1). The study area is approximately 47.59 km^2 and has an estimated population of 105, 628 (Jigawa State Government, 2017). The built-up portion is positioned north of the Hadejia River and resides upstream from the Hadejia-Nguru wetlands, facilitating irrigation farming but posing a significant risk of flooding. Hadejia is in a semi-arid region known for its prolonged dry season (November–May) and brief wet season (June/July–October). The dry season planting (Fadama or irrigation farming) is mainly for rice, wheat, and vegetables. The crops grown during the rainy seasons are rice, maize, millet, and sorghum (Bush, 2012; Food and Agriculture Organization (FAO), 2023c).

2.2. Data

This research employed data from multiple sources (Table 1).

2.2.1. Rainfall data

The dataset contains daily rainfall amount measurements recorded by a rain gauge in the study area, obtained from the Nigerian Meteorological Agency (Nigerian Meteorological Agency (NiMet), 2023). The rainfall data covers the period 2012 to 2022 and is presented in a structured spreadsheet format. This dataset plays a crucial role in examining rainfall patterns and evaluating climate variability.

2.2.2. PlanetScope

PlanetScope (PS) is a constellation of 130 satellites (as of 2023) that offers multi-spectral daily high-resolution satellite imagery of 3m globally. It provides orthorectified images at different processing levels (visual, top of atmosphere, and surface reflectance) and a spectral resolution of 4 bands (RGB, NIR) or 8 bands (RGB, NIR, Red Edge, Yellow, Green I, and Coastal Blue) (Table S1), which are helpful for land cover mapping, crop yield and growth monitoring, disaster and climate change assessment, and other applications. (Planet Labs, 2023b; Roy et al., 2021).

Table 1
Data sources.

S/N	Data	Purpose	Spatial Resolution	Period	Source(s)
1	Reports on flood incidents	Determine dates of flood events to filter satellite image selection	__	2020–2022	(Associated Press, 2022; Daily Post, 2020; Daily Trust, 2020; Floodlist, 2022; National Emergency Management Agency (NEMA), 2023; Premium Times, 2022a)
2	PlanetScope MSI	Land cover classification. Flood extent & progression mapping	3m	2020 & 2022	(Planet Labs, 2023a)
3	Sentinel-2 MSI	Flood extent accuracy assessment. Crop recovery classification. NDVI trend analysis	10–60m	2020 - 2023	(European Space Agency (ESA), n.d.)
4	Sentinel-1 SAR	Flood extent & progression mapping	10m	2020 & 2022	(European Space Agency (ESA), n.d.)
5	Harmonized Landsat Sentinel (HLS)	NDVI trend analysis	30m	2020 & 2023	(National Aeronautics and Space Administration (NASA), 2023)
6	Rainfall	Rainfall distribution pattern	__	2012–2022	(Nigerian Meteorological Agency (NiMet), 2023)
7	Copernicus DEM GLO-30.	Examine the effect of terrain on flooding dynamics	30m	2006	(European Space Agency and Airbus, 2022)
8	Administrative boundary	Delineate study region extent	500m	2015	(Food and Agriculture Organization (FAO), 2015)
9	Survey/participatory mapping data	Crop damage assessment and validation of EO crop recovery results. Impacts of flooding on farmers	__	2020 & 2022	Authors and Field Survey Assistants

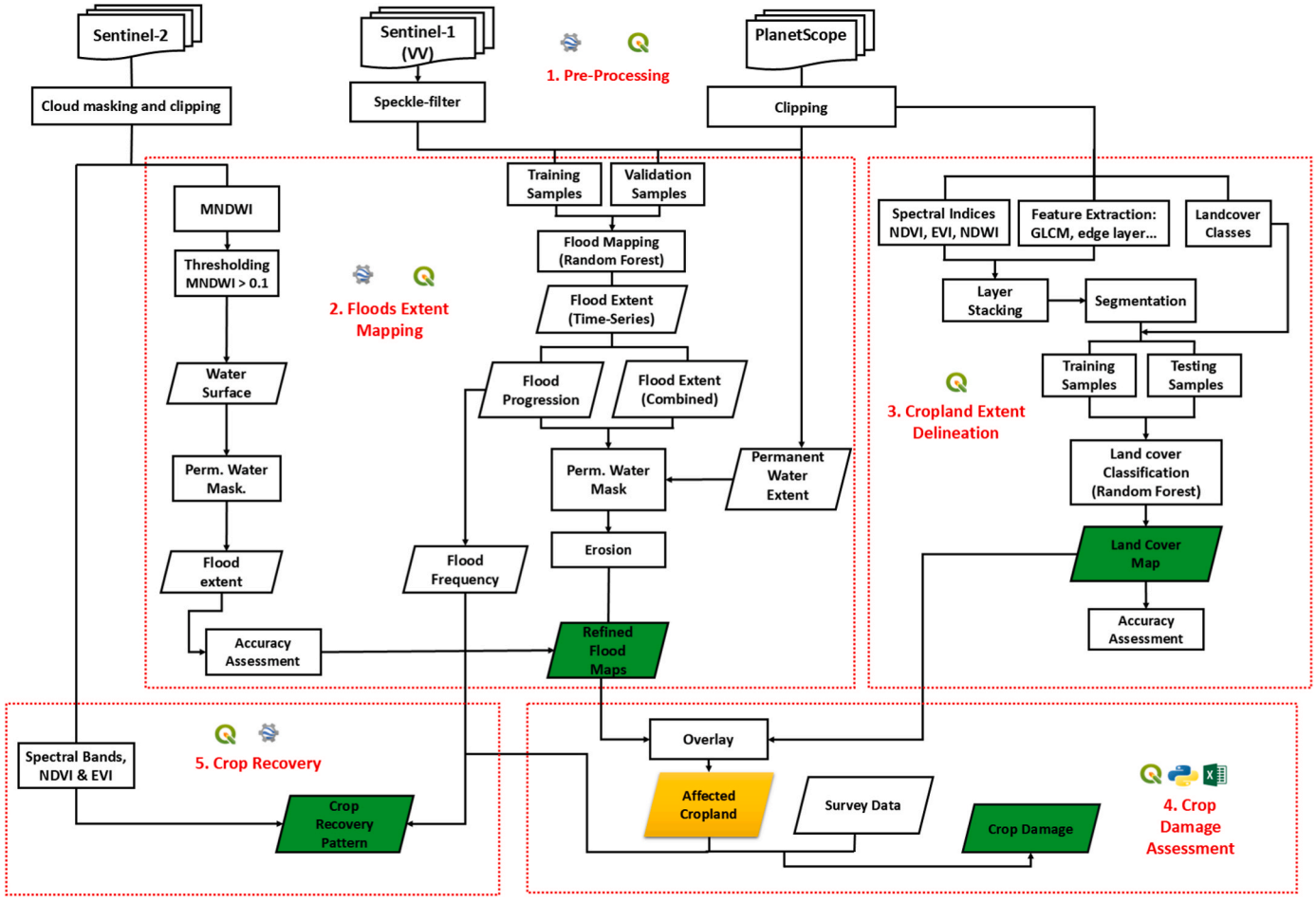

Fig. 2. Methodological framework.

2.2.3. Sentinel-1

Sentinel-1 (S-1) is part of the European Space Agency (ESA) satellite constellation, which is a Synthetic Aperture Radar (SAR) twin satellites (Sentinel-1A/B) of C-band with a frequency of 5.4 GHz (Torres et al., 2012). The S-1 offers images in Strip map (SM), Interferometric Wide Swath (IW), Extra Wide Swath (EW), and Wave (WV). It has a temporal resolution of 6 or 12 days, depending on the locations, and a spatial resolution of 10m, 25m, or 40m. The S-1 image comes in four polarizations. The S-1 Ground Range Detected (GRD) collection in the Google Earth Engine (GEE) cloud computing platform consists of Level 1 Ground Range Detected (GRD) scenes with backscatter coefficient values in decibels (dB), and it has been corrected for thermal noise, terrain effects, and radiometric calibration.

Table 2
Satellite imagery and processing for flooding mapping.

	Optical		Microwave SAR
Dataset/ Sensor	PlanetScope MSI, 8b SR	Sentinel-2 MSI, L2 SR	Sentinel-1 SAR GRD (VV)
Number of images	2020: 4 images. 2022: 8 images.	2020: 6 images. 2022: 10 images.	2020: 7 images. 2022: 4 images.
Date	September 25, 2020, October 04, 2020, October 12, 2020, & October 28, 2020. August 07, 2022, September 20, 2022, September 26, 2022, September 28, 2022, October 01, 2022, October 08, 2022, October 18, 2022, & October 28, 2022.	August 17, 2020, September 26, 2020, October 06, 2020, October 11, 2020, October 16, 2020 & October 31, 2020. August 07, 2022, September 06, 2022, September 11, 2022, September 26, 2022, October 01, 2022, October 11, 2022, October 16, 2022, October 21, 2022, October 26, 2022, & October 31, 2022.	August 14, 2020, August 26, 2020, September 07, 2020, September 19, 2020, October 01, 2020, October 13, 2020, & October 25, 2020. August 04, 2022, August 16, 2022, August 28, 2022, & September 09, 2022.
Spatial resolution (m)	3	10	10
Pre-processing		Cloud-masking.	Speckle filter (50m). Resampling to 3m.
Composition	Time series images.	Time series images.	Time-series images (RF) & monthly composites images (CDAT).
Method of analysis	RF	MNDWI	RF & CDAT.

Table 3
Satellite images for land cover classification, number of bands, indices, features, and resolution.

	Factor	PlanetScope (Bands & Derived variables)	Description
Date	—	July 26, 2022	—
Spectral bands	Mean and standard deviation (B2 – B8). Variance (B7).	B2, B3, B4, B5, B6, B7, B8	—
Spectral indices	Mean and standard deviation.	NDVI, NDWI	(B8 – B6)/(B8 + B6), (B4 – B8)/(B4 + B8)
Texture	Mean and standard deviation.	Sobel edge, Cluster Shade	—
Resolution (m)	—	3	—

Table 4
Land cover nomenclature.

S/N	Land cover	Description
1	Bare soil	Barren land without buildings or vegetation.
2	Built-up	Buildings, human settlements, and roads.
3	Cultivated land	Agricultural land that is cultivated.
4	Fallow land	Agricultural land that is not cultivated at that moment.
5	Tree & Grass	Trees, shrubs, and grasslands.
6	Water & Wetland	Rivers, streams, ponds, and wetlands.

Table 5
Uniform intervals for the flooding periods.

	2020	2022
Day 1	14 Aug	04 Aug
Day 4	—	07 Aug
Day 13–25	26 Aug to 07 Sept	16 Aug to 28 Aug
Day 37–48	19 Sept to 01 Oct	09 Sep to 20 Sep
Day 54–66	04 Oct to 13 Oct	26 Sep to 08 Oct
Day 76–86	25 Oct to 28 Oct	18 Oct to 28 Oct

Table 6
Predictor variables for the crop recovery status analysis.

Variable	Description
Red_edge_max	Maximum value of B5 in S-2 image collection.
NIR_max	Maximum value of B8 in S-2 image collection.
SWIR_max	Maximum value of B11 in S-2 image collection.
SWIR_max	Maximum value of B12 in S-2 image collection.
Red_min	Minimum value of B4 in S-2 image collection.
Green_min	Minimum value of B3 in S-2 image collection.
Blue_min	Minimum value of B2 in S-2 image collection.
EVI_max	2.5*(NIR - Red)/(NIR + 6*Red - 7.5*Blue + 1).
NDVI_max	Maximum value of (NIR - Red)/(NIR + Red) in S-2 image collection.
Flood Frequency	Equation (4).

max: maximum. min: minimum.

2.2.4. Sentinel-2

Sentinel-2 (S-2) is an ESA multispectral satellite with twin satellites (Sentinel-2 A/B) launched in 2015 and 2017, respectively. It is part of the land monitoring mission from the European Union (EU) Copernicus Programme, which has a temporal resolution of 5 or 10 days; 10 days at the equator with one satellite, while employing two satellites increases the temporal frequency to 5 days, yielding 2–3 days of observation at mid-latitudes. The S-2 image has 13 spectral bands. The visible and near-infrared bands of the S-2 images are available at 10m spatial resolution, while the resolution of the other bands is either 20m or 60m (Table S2). These images are available in both Bottom-of-Atmosphere or surface reflectance (Level-2A) and Top-of-Atmosphere (Level-1C) (European Space Agency, n.d.).

2.2.5. Global administrative unit layers (GAUL)

The Global Administrative Unit Layers (GAUL) by the Food and Agricultural Organization (FAO) of the United Nations (UN) contained detailed information on administrative boundaries worldwide. The multi-polygon layers' attributes are defined with consistent coding systems across multiple administrative levels. The FAO GAUL boundary data was used in this study because it has been proven to be the most reliable boundary data in terms of accuracy and completeness, especially in African countries (Brigham et al., 2011; Food and Agriculture Organization (FAO), 2015).

2.2.6. Participatory mapping/survey data

A Google form was designed and administered to the farmers on their farms between 1st and October 8, 2023 to collect the survey data. The questions in the Google form were read to farmers, and their responses were entered into the form. Data was collected on their farming practices, experience with flooding and its damaging effects on their livelihood, and coping strategies and mitigation measures (Table S3). The survey data is geo-located with pictures (Fig. S1).

2.3. Methods

The methodological framework used in this research is depicted in Fig. 2, and explanations follow.

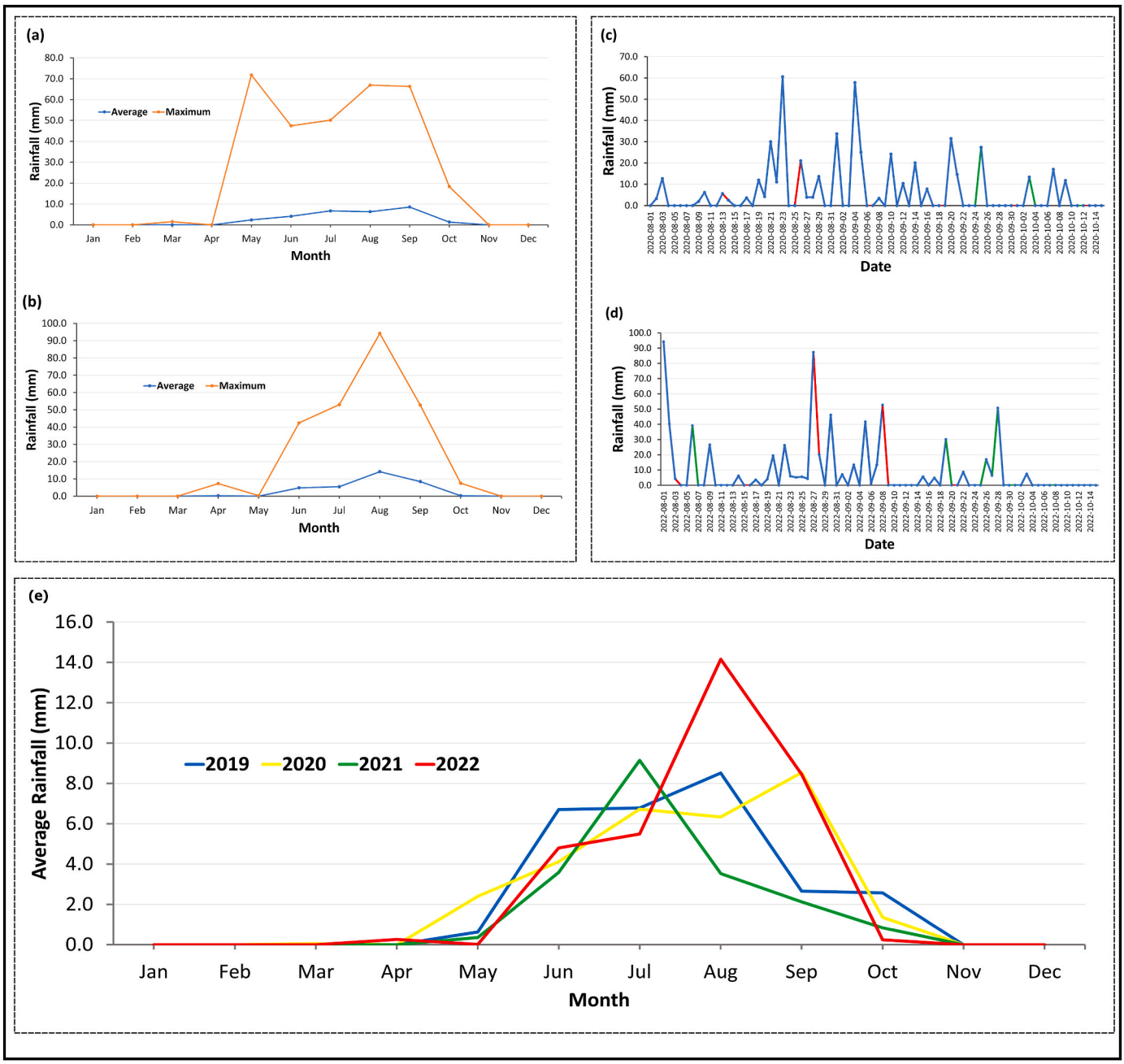

Fig. 3. Monthly average and maximum rainfall in (a) 2020, (b) in 2022, (c) daily rainfall distribution between August and October in 2020, (d) daily rainfall distribution between August and October in 2022, and (e) rainfall pattern from January to December of 2019–2022. In panels c & d, the red colour symbolizes the dates of the S-1 images and the green colour represents the dates of the PS images used for the flooding mapping. (Rainfall data source: NiMet (2023)).

2.3.1. *Rainfall distribution*

The rainfall data was analyzed to understand the influence of rainfall patterns and variations on flood occurrence and duration. The rainfall data was reduced to the monthly average to identify the months with high rainfall records using Microsoft Excel. An exploratory analysis of the daily rainfall during flood months was conducted to examine rainfall variation and relate it to the news reports of flood occurrences. This assisted in the selection of images to capture the flooding dynamic.

2.3.2. *Flood extent and progression from multi-source satellite images*

The cloud cover percentage and insights on the flood events, derived from the rainfall pattern and news reports (Associated Press, 2022; Daily Post, 2020; Floodlist, 2022), were considered in selecting satellite images for flood mapping. Although SAR images are often preferred for flood mapping due to their resistance to clouds (Long et al., 2014), the available S-1 SAR images did not fully capture the dynamic flooding patterns in the study area. Thus, both time series cloud-free optical PS and SAR S-1 images were used for flood mapping, while optical S-2 images were utilized for the accuracy assessment of the flood layers derived from PS and S-1 images. The S-1 images were pre-processed in GEE (Gorelick et al., 2017), which included a 50m radius filter to reduce speckle effects and clipping to the study area extent. The processed images were exported for further analysis in QGIS. The PS images were downloaded from the Planet Lab website at the surface reflectance processing level. For each satellite image, a different set of training and validation sample data was created by visually inspecting the images and drawing polygons to represent the "flooded" and "non-flooded" groups of pixels (Fig. S2). The Random Forests (RF) algorithm, a robust

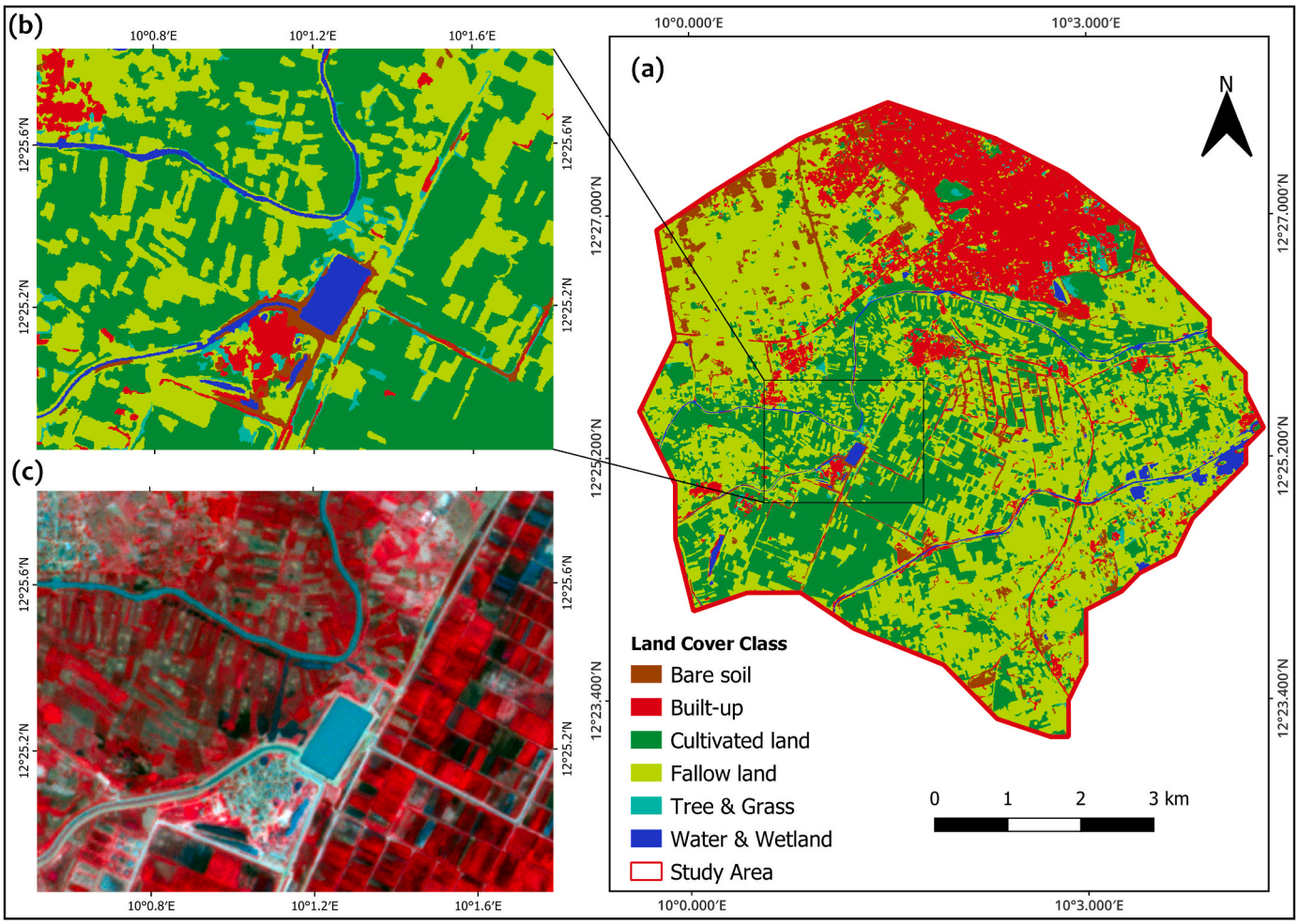

Fig. 4. (a) Land cover map, (b) zoom extent from the land cover map, and (c) PlanetScope False Colour Composite (FCC) image of the zoom extent.

Table 7
Land cover classes and their areas.

Id	Land cover	Area (km^2)	Percentage (%)
1	Bare soil	1.98	4.16
2	Built-up	6.57	13.80
3	Cultivated land	14.26	29.96
4	Fallow land	22.89	48.11
5	Tree and Grass	1.01	2.11
6	Water & Wetland	0.89	1.86
	Total	47.59	

supervised classifier (Maxwell et al., 2018), was used to classify each PS and S-1 image into the binary class of "flooded" and "non-flooded." The Orfeo Toolbox (OTB) in QGIS was used to implement the RF algorithm using the "Image Classifier" tool. Eleven images (7 S-1 and 4 PS) were used to generate eleven flood layers showing the progression of the flooding in 2020. Similarly, twelve images (4 S-1 and 8 PS) were used to produce twelve flood progression layers for 2022 (Table 2). The union of the flood layers from the time series images represented the total/-maximum flooded extent for 2020 and 2022, respectively. Then, the permanent water body was digitized from the PS image of May 2022 because it is between the driest and rainy months and was subsequently masked out from the flood extent layers to generate the refined flood extent layer. Erosion morphological operation was applied to reduce the noise in the flood extent layer. The VV polarization of the S-1 image was used because of its lower backscattering coefficient of water bodies, which makes it appear dark in a VV-polarized image, and better discriminate between wet and dry surfaces because of its sensitivity to surface roughness (Clement et al., 2018; Manjusree et al., 2012).

To verify the accuracy of the flood extents derived from S-1 and PS images using the RF method, the water surface (permanent water and flood water) was generated from time-series S-2 images using MNDWI (Equation (1)) and thresholding (MNDWI >0.1). Thresholds greater than 0 are widely used to extract water surface from MNDWI layer (Cian et al., 2024; Xu, 2006), and the threshold value of 0.1 was used after iterative trials of threshold values. The permanent water extent was masked to extract just the flood extent. Then, 300 random test points were generated each for 2020 and 2022, and their corresponding values (flooded or non-flooded) from the MNDWI (S-2) and RF (S-1 and PS) flood extent layers were evaluated for the accuracy assessment (Fig. S3). This validation approach has been found to be reliable in previous studies (Clement et al., 2018; Michael et al., 2023). The S-2 images were downloaded and processed in GEE.

$$MNDWI = \frac{GREEN - SWIR}{GREEN + SWIR} \quad (1)$$

where GREEN is band 3 of Sentinel-2, and SWIR is band 11.

The CDAT technique was also tested for the flooding extent mapping using the S-1 minimum monthly composite images from August, September, and October during the flood events, along with a median composite of all pre-flood images. These composites were used to compute the different images (Equation (2)). The minimum composite is the lowest pixel value extracted from the image, which indicates the lowest backscatter values, as water exhibits low backscatter in SAR

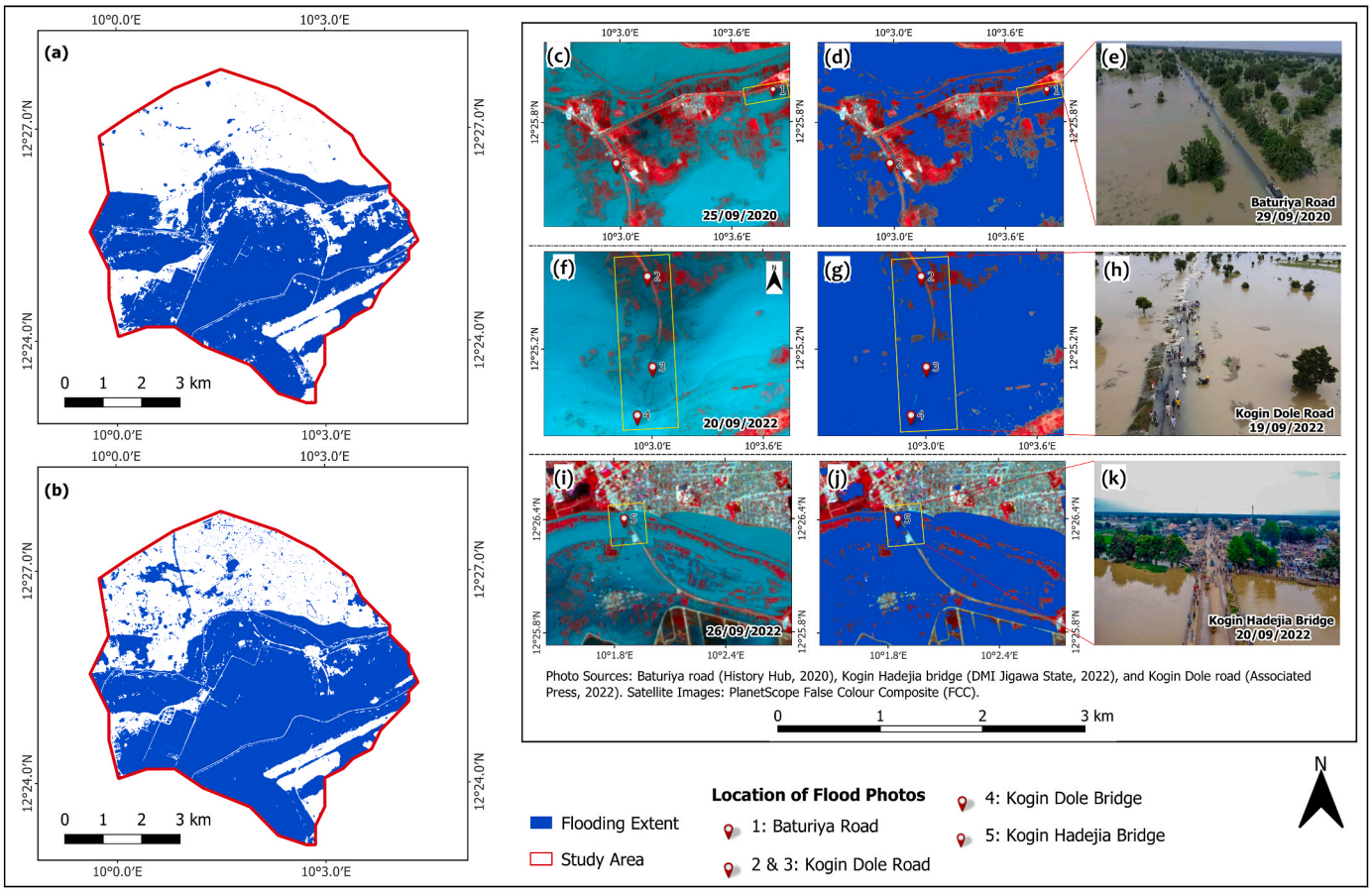

Fig. 5. (a, b) Flood extents in 2020 and 2022, (c, f, i) PlanetScope FCC image of some portions of the flooded area, (d, g, j) classified flooding extent of the portions, and (e, h, k) photos of the flooded portions. (Photo Sources: Baturiya road (History Hub, 2020), Kogin Hadejia bridge (DMI Jigawa State, 2022), and Kogin Dole Road (Associated Press, 2022)).

images. The difference image (D) was calculated by subtracting the median composite of the pre-flooding (R) from each of the minimum composites of the flooding (F). Flooded pixels were then detected by applying a threshold (Equation (3)) after masking areas with a slope greater than 5°.

$$Difference\ (D) = |F| - |R| \tag{2}$$

$$Pf\ < (\{\mu[D]\} - fc^{*}\{\sigma[D]\}) \tag{3}$$

where (D) is the absolute difference image, R is the composite of the pre-flood image, and F is the composite of the flooded image. P_f is the flooded pixel, μ and σ are the mean and standard deviation of the difference image (D), and *fc* is the coefficient. The optimum value of fc is obtained through iterative trials or using a value of 1.5 (Long et al., 2014). The CDAT was implemented in the GEE cloud computing platform (Gorelick et al., 2017).

2.3.3. Cropland extent delineation from high-resolution image

The closest cloud-free PS image to the commencement of the flooding event in 2022 was used for the land cover classification to ensure it accurately represented recent conditions of the land cover. A data fusion approach was used by integrating PS image spectral bands with spectral indices, edge layer, and textural features (Table 3). The land cover classification was performed using the Object-Based Image Analysis (OBIA) technique. First, sample points representing six land cover classes (Table 4) were generated using point features on the satellite image. Then, the Large Scale Mean Shift (LSMS) tool in the OTB plugin in QGIS was used for the segmentation of the PS image. The segmentation process requires two essential input parameters: spatial radius (pixels) and range radius (μm). The segmentation results in image objects (polygon segments), in which neighbouring pixels with a range distance less than the specified range radius and a spatial distance less than the specified spatial radius were combined into a single cluster. Next, the zonal statistics (mean, standard deviation, and variance) were computed on the raster image to ensure the segments have the spectral properties of the image. The segments were then joined with the point features representing land cover classes using the "Join Attribute by Location" function in QGIS. This process ensured that each segment was assigned a land cover label. Segments without corresponding point features were discarded. The joined segments were randomly split into training (70 %) and validation (30 %) sets (Fig. S4). The vector classifier tool in OTB was used to implement the learning of the model to generate the land cover map. Lastly, the accuracy of the land cover layer was assessed using 160 random testing points (Fig. S5). These reference points were labelled using Google Satellite and PlanetScope images. The corresponding values of the land cover layer were extracted for these random testing points using the "Point Sampling Tool" in QGIS.

2.3.4. Cropland damage assessment

The flooded cropland in 2020 and 2022 were identified by overlaying the cropland extent and flood extent layers for each respective year. Also, the time-series flood progression layers at different time ranges in the cropland region were combined for 2020 and 2022, respectively (Table 5). This was used to estimate the extent of the flooded cropland while accounting for the dynamic nature of the flooding. More so, two flood frequency layers were generated to examine the degree (magnitude) of damage suffered by the farmers due

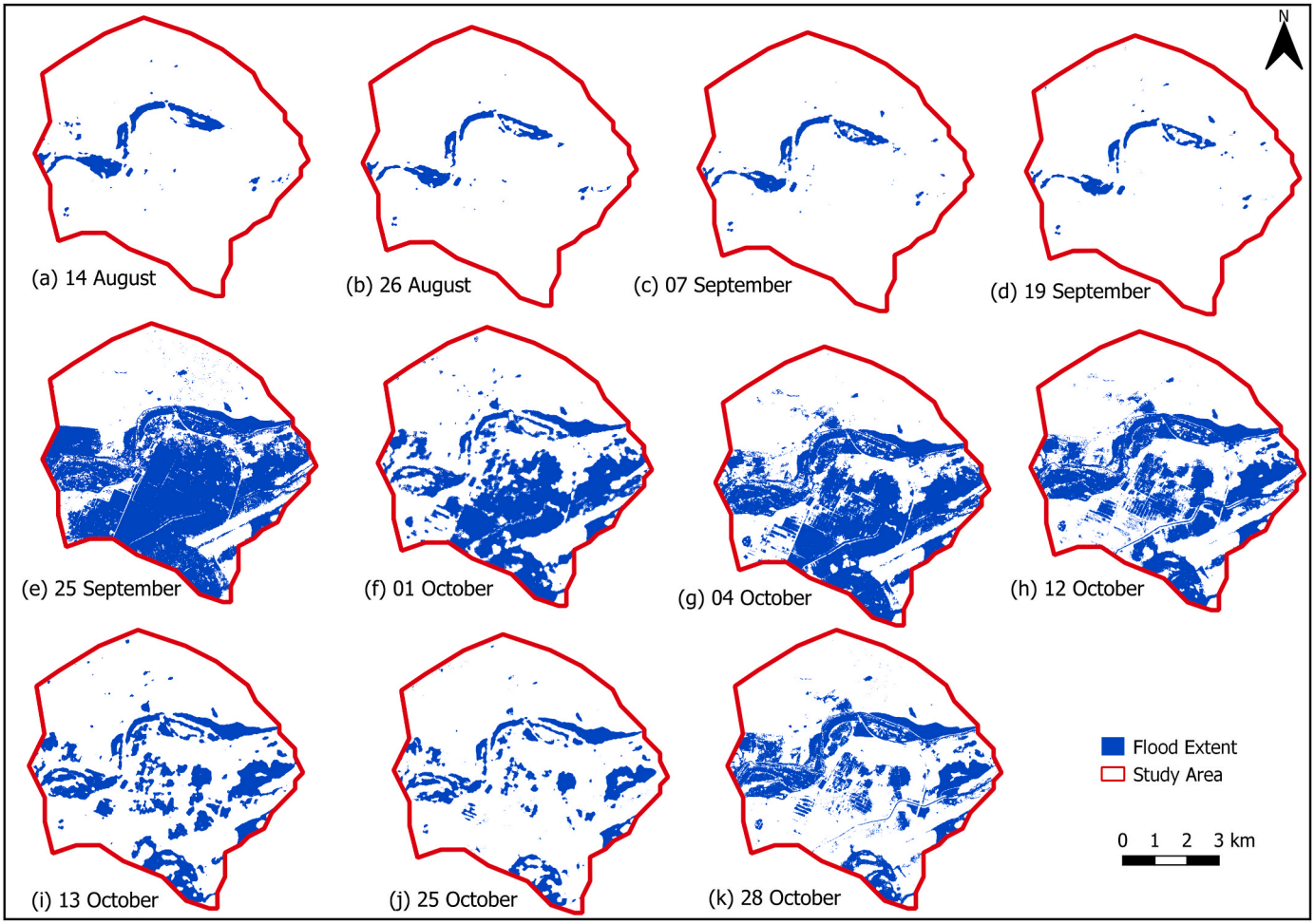

Fig. 6. Flooding progression in 2020.

to the flooding. Flood frequency refers to the number of times a specific location (pixel) experiences flooding over a given period. It is represented as a flood frequency layer, which was derived by summing all time-series flood progression layers —individual flood extent layers from Sentinel-1 (S-1) and PlanetScope (PS) images that were clipped to the affected cropland extent— and normalized by the total number of images analyzed (Equation (4)). Separate flood frequency layers were generated for 2020 and 2022 (Equations S1 & S2). The flood frequency values correspond to the number of images (section 2.3.2): 1 to 11 for 2020 and 1 to 12 for 2022. A value of 1 indicates that a pixel was flooded once, whereas a value of 12 indicates that the pixel was flooded 12 times. This process was done using the "Raster Calculator" function in QGIS.

$$F = \frac{\sum_{i=1}^{N} Li}{N} \quad (4)$$

where F = Flood frequency, Li = Binary flood layer for image (1 is flooded pixels, 0 not flooded pixels), N = Total number of flood layers (images).

The flood frequency layers, flood progression layers, and data from the participatory mapping (Section 2.3.6) were used to estimate the number of days that a rectangular cropland plot (data point from the participatory mapping) was flooded. The participatory mapping data is geolocated point data and contains three damage levels the farmers indicated: minimal, moderate, and severe. A rectangular buffer of 30m × 15m was created because the croplands are polygon features (Fig. S6). This dimension reflects the minimum farmland size recorded in the survey and aligns with the general definition of cropland (Waldner et al., 2016).

Zonal statistics were then computed to extract the "majority value" of the flood frequency for each rectangular cropland plot, indicating how often a cropland plot was flooded. Then, the flood progression layers for 2022 (12 layers) were stacked into a composite layer. A similar zonal statistics approach was applied to this stacked flood progression layer to determine the first date each rectangular cropland plot experienced a flood. Combining the first date that a rectangular cropland plot was flooded with the number of times it was flooded was used to determine the number of days a rectangular cropland plot was flooded. This process was done for 2022 alone because the survey data on damage levels was reported for 2022.

2.3.5. *Crop recovery from satellite image and participatory mapping*

To assess the recovery pattern of the crop, time-series statistical averages of NDVI of the flooded cropland were generated from time-series cloud-masked S-2 images in GEE from January to December (2020–2023). These values were plotted in a line chart. The trend of the NDVI before, during, and after the flood's peak was analyzed to determine an appropriate reference date for assessing cropland recovery classification with ML. In both years, NDVI showed a noticeable increase on October 11th, suggesting early signs of crop recovery. Therefore, S-2 images from October 11th were selected as reference images for classifying cropland recovery in 2020 and 2022. To train the RF classification ML algorithm, sample point data was randomly selected and labelled by visual observation of the S-2 images of October 11th. 64 samples were used for training the model for the crop recovery classification in 2020

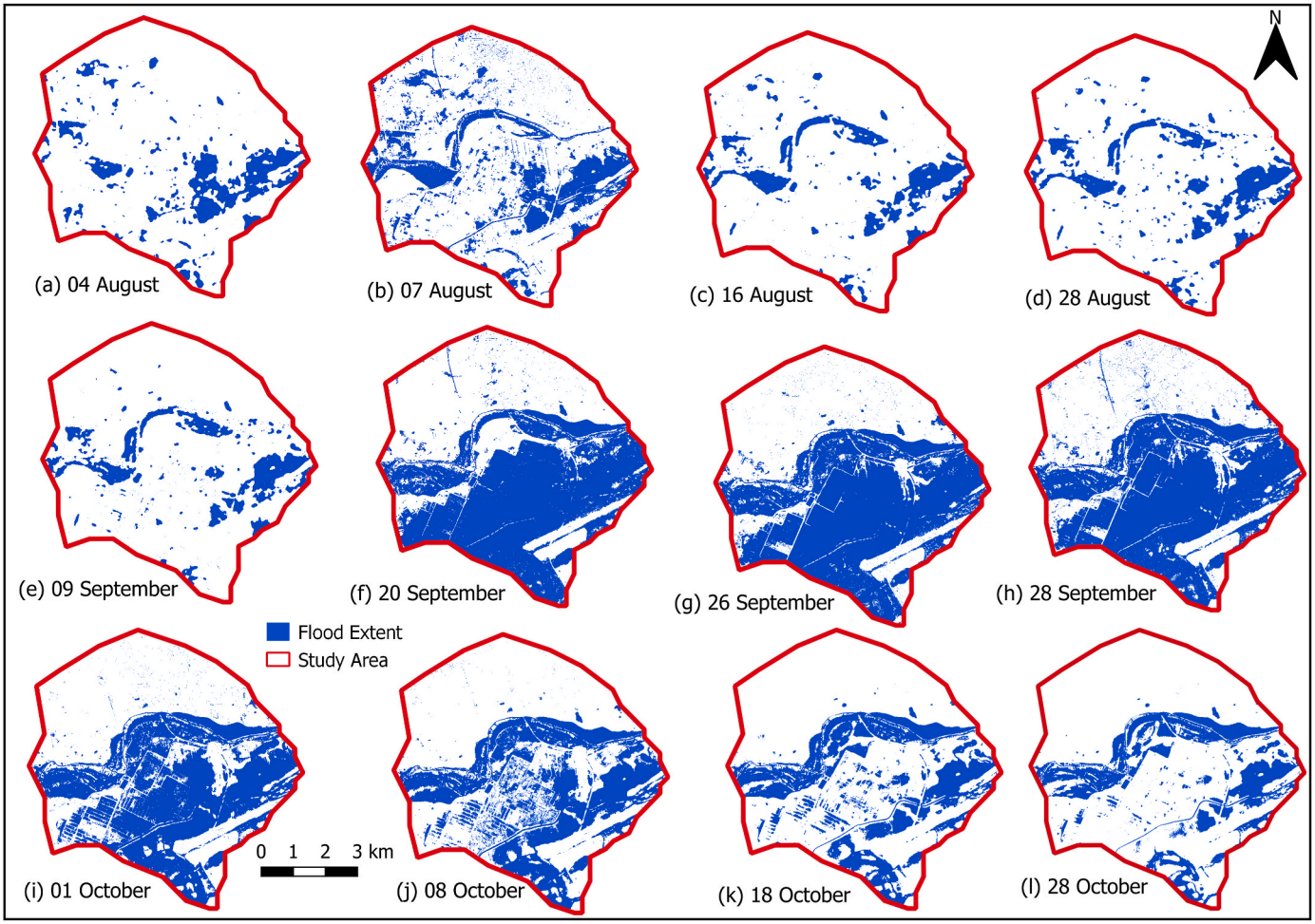

Fig. 7. Flooding progression in 2022.

and 94 samples in 2022. 26 samples were used to test the crop recovery classification model in 2020, while 57 samples were used for testing in 2022. Ten variables (Table 6) were used as predictors to classify the flooded cropland as either recovered or unrecovered in the GEE environment. This method is similar to that adopted by M. Li et al. (2022b). Three recovery classes were defined for the classification: recovered, unrecovered I, and unrecovered II.

i. The "recovered" class represents flooded cropland showing visible greenness, indicating the presence of recovered crops.
ii. "Unrecovered I" refers to areas where the greenness in the cropland has disappeared, possibly due to premature harvesting or total crop damage, but there are no visible signs of floodwater.
iii. "Unrecovered II" represents cropland with the presence of flooding water.

All three recovery classes are based on conditions observed after the peak of the flood. The predictor raster layers were all resampled to 3m using the nearest neighbours to match the spatial resolution of the flood frequency layer.

To analyze the agreement between the crop recovery classification from the remote sensing approach and the farmers' reported loss in the participatory mapping data, the participatory mapping data was refined from 202 to 197 entries (Section 3.5). This subset comprised farmers who reported that they experienced total crop loss from the 2022 flood and whose dominant raster-sampled values (from the recovery classification layer) fell within the three defined recovery classes.

2.3.6. *Participatory mapping data processing*

Two hundred and seventy (270) responses were recorded from the participatory mapping. The following pre-processing was performed on the data in a Python environment: conversion of the area of farmland from text (string) to numeric data type, conversion of the area of the farmland to a standard unit (hectare), removal of points that are not within the boundary of the study region, and removal of cells where damaged cropland area is greater than the cultivated area. Further analysis was carried out on the cleaned data to compare the results of the degree of damage to the results from EO data.

3. Results

3.1. *Rainfall distribution pattern*

The highest monthly average rainfall in 2020 and 2022 was in July, August, and September (Fig. 3a and b). The daily distribution of rainfall patterns shows continuous rain from August to September for both years, with the red and green colours symbolizing the dates of the S-1 and PS images used for the flooding mapping (Table 2), respectively (Fig. 3c and d). The highest daily rainfall (69.40 mm) recorded in 2020 was in May, which is the only rainfall for the month (Fig. 3a). The rainfall on 1st August (94.20 mm) was the highest in 2022 (Fig. 3b). A similarity can be seen in the pattern of rainfall in August and September of both years, particularly in late August and early September. There is a high intensity of rainfall in August and September of 2020 and 2022 (the flood years) compared to 2021, when there were no floods (Fig. 3e).

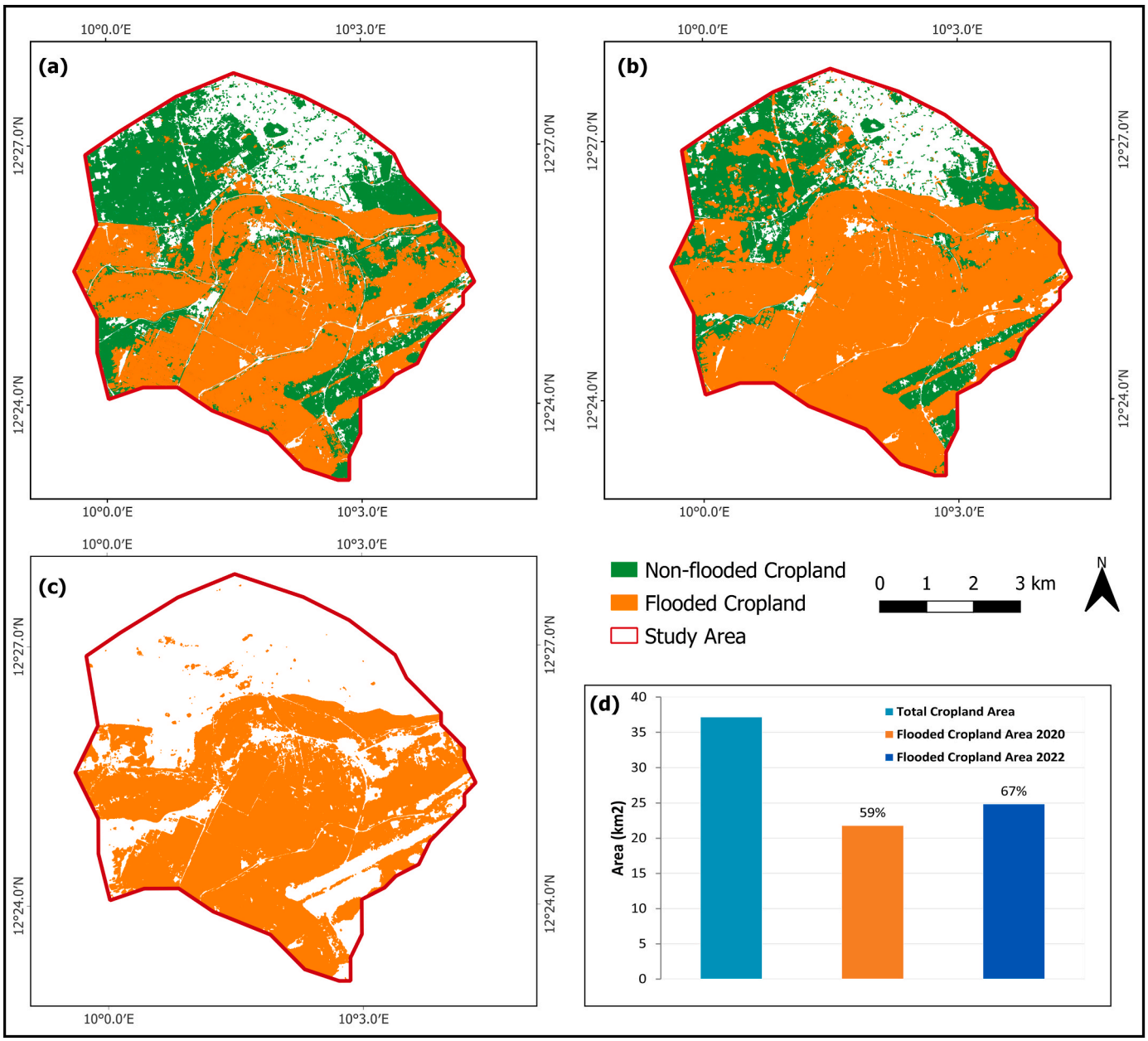

Fig. 8. The extent of the flooded cropland in (a) 2020, (b) in 2022 (c), common to both 2020 and 2022, and (d) statistical areas of total cropland and flooded cropland.

3.2. Cropland extent

The land cover map is shown in Fig. 4. The dominant land cover class is Fallow land (22.89 km^2), followed by cultivated land with 14.26 km^2 (Table 7). This is because the date of the image used for the classification was the period when the common crops (rice and millet) cultivated in the dry season are harvested, and new seeds are sowed for the rainy season. For subsequent analysis, the cultivated land and fallow land classes were merged into a single "cropland" class. The total cropland area is 37.15 km^2, which constitutes 78 % of the total study area, indicating that the study area is predominantly agrarian.

3.3. Spatial and temporal distribution of flooding from multi-source satellite images

The refined combined/maximum flooding extent maps revealed that 23.65 km^2 (50 % of the study region) was flooded in 2020, while 27.22 km^2 (57 %) was flooded in 2022 (Fig. 5a and b). Similar geographic portions of the study region were flooded in both years. Some of the most severely impacted areas during the peak of the floods include Baturiya Road, Kogin Dole Road, and Kogin Hadejia Bridge (Fig. 5c–k).

The flood progression maps (Figs. 6 and 7) show the dynamics of the flood events in 2020 and 2022, respectively. The images used for the flooding progression maps are depicted in Fig. S7 and S8. In 2020, the flood began in mid-August (Fig. 6a). The peak of the flooding was on 25 September (Fig. 6e). Similarly, in 2022, the first flood event was on 4 August, while the peak of the flooding was between 20 and 26th September, as captured on the PS image (Fig. 7f and g). There are still traces of the flooding water and deeply moisturized soil in late October (Fig. 7i). The period of the flooding commencement and peak observed on the satellite images correspond to the reports in the news media (Associated Press, 2022; Floodlist, 2022; The Cable, 2022).

There is a noticeable difference in the spatial dynamics of the flood extents in 2020 and 2022. At the early stage of the flood in 2020 and

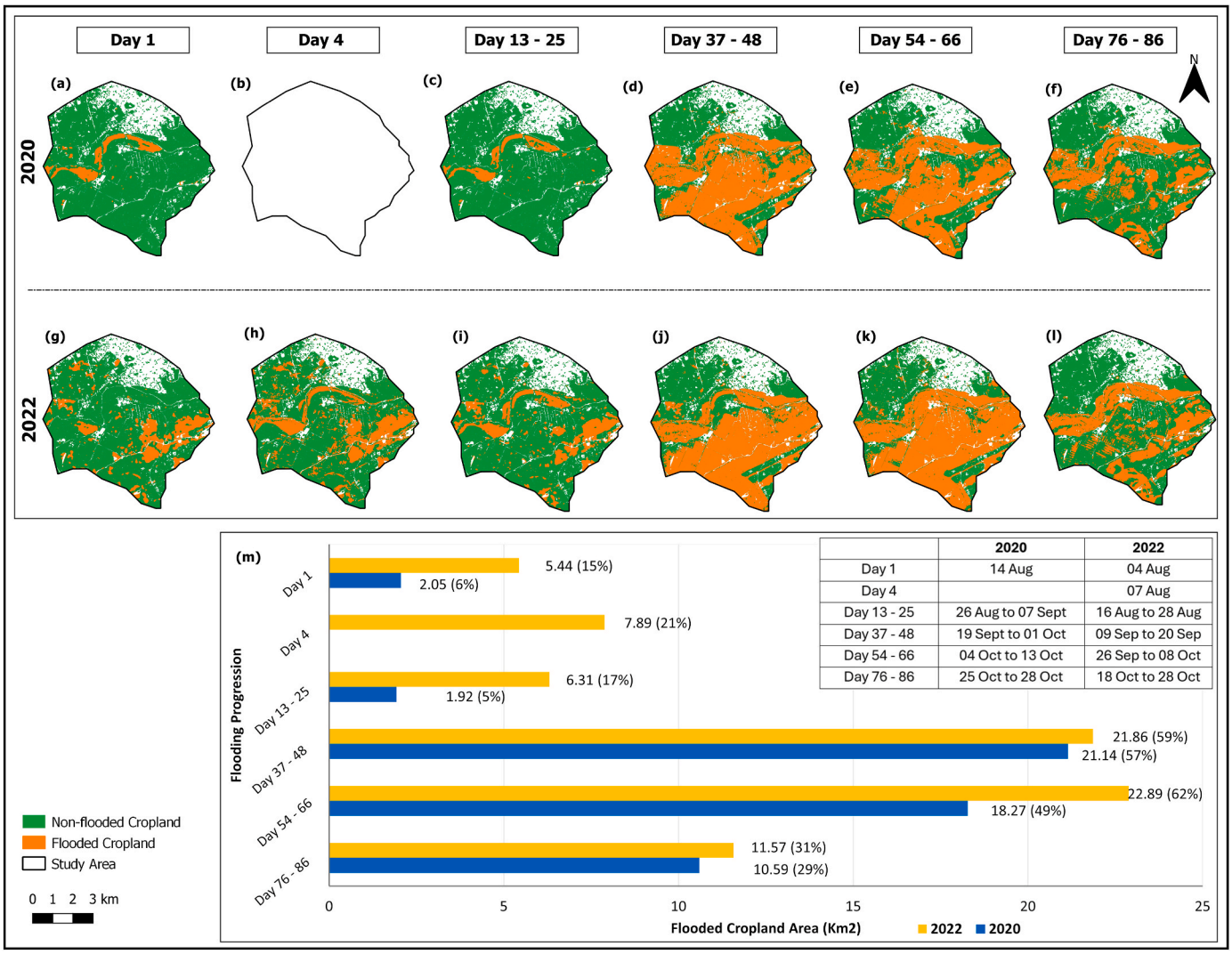

	2020	2022
Day 1	14 Aug	04 Aug
Day 4		07 Aug
Day 13 - 25	26 Aug to 07 Sept	16 Aug to 28 Aug
Day 37 - 48	19 Sept to 01 Oct	09 Sep to 20 Sep
Day 54 - 66	04 Oct to 13 Oct	26 Sep to 08 Oct
Day 76 - 86	25 Oct to 28 Oct	18 Oct to 28 Oct

Fig. 9. Affected cropland extents at different flooding periods. The blank image in 9b is due to missing satellite data for day 4 in 2020 (Table 5).

2022 (Fig. 6a–d and 7a-d), only the northern and eastern parts of the study region were flooded, and the flood had not yet reached most of the cropland in the central area. The flood began to affect the central cropland more significantly during the peak of the flooding in September (Fig. 6e and 7f). Also, the result of the flood extent from CDAT underestimated the flood extent (Figs. S9, S10, and S11), and thus, it was not used in the analysis.

3.4. Crop damage and flood durations

The result of the flood damage analysis for the cropland is presented in Fig. 8, and the damage area for other land cover classes is shown in Fig. S12. In 2020 and 2022, 21.79 km^2 (59 %) and 24.85 km^2 (67 %) of cropland were flooded, respectively (Fig. 8a, and b). This represents 92 % and 91 % of the total flooded area. A total of 20.56 km^2 (55 %) of cropland was affected by flooding in both 2020 and 2022, representing spatial overlap between the two flood events (Fig. 8c and d).

Fig. 9 illustrates the damage assessment in relation to flood duration. In both 2020 and 2022, only a small portion of cropland was initially affected by the first flood event (Fig. 9a and g). As flooding persisted between the 37th and 48th days, cropland inundation increased to 57 % in 2020 and 59 % in 2022. This period corresponds to when most portion of the cropland, particularly in the central and southern parts of the study region, experienced the first flood and aligns with the peak flooding phase in 2020 (Fig. 6). A more significant portion of the cropland (62 %) was inundated in 2022 as the flooding reached its 66th day, coinciding with the flood peak (Fig. 7g), and this is the peak of the growing stage and near harvesting time of the rain-fed crop (Bush, 2012; Food and Agriculture Organization (FAO), 2023c). After the flood peaks in both years, the flooded extent decreased to approximately 30 % of the study region. However, some cropland areas remained flooded until the 76th day after the flooding began, which was in late October.

3.5. Degrees of cropland damage

After pre-processing and data cleaning, the participatory mapping dataset was initially reduced from 270 to 227 entries (Section 2.3.6). Subsequently, the raster zonal statistics analysis was used to exclude data points/rectangular cropland plots (Fig. 10a) that did not intersect with the combined flood extent, flood frequency, and crop recovery layers of 2022. This refinement further reduced the participatory mapping dataset to 202 entries. The result from the participatory mapping, based on the farmers' reports, indicated that 23 (11 %) rectangular cropland plots experienced moderate damage, while 179 (89 %) rectangular cropland plots suffered severe damage because of flooding in 2022. Spatial analysis using the participatory mapping data with the flood progression layer (Figs. 6 and 7) and flood frequency layer (Fig. 10a) shows that most of the rectangular cropland plots that were

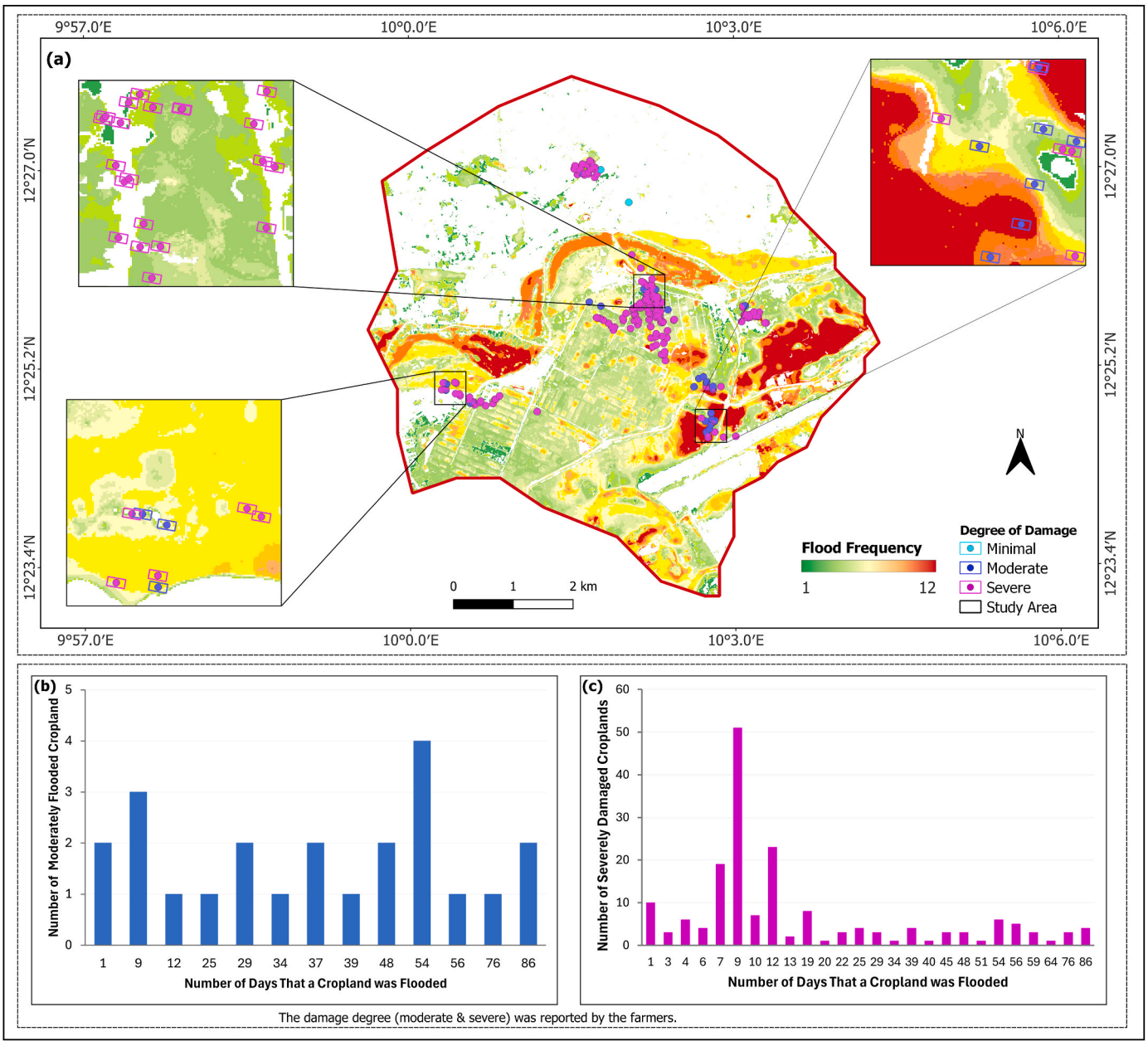

Fig. 10. (a) Participatory mapping data points and buffered polygons of crop plots coloured by degrees of damage overlaid on the flood frequency layer in 2022, (b) number of days that croplands were flooded according to moderately damaged, and (c) severely damaged.

reported to be severely damaged by the farmers were flooded for 54 days. Also, most of the severely damaged croplands were flooded for 9 days, while some farmers reported severe damage even when their fields were inundated for just 1 day. Moreover, there are rectangular cropland plots that were inundated for as long as 86 days in both categories (Fig. 10b and c).

3.6. Crop recovery pattern

Monitoring crop development conditions has been greatly enhanced by the use of Vegetation Indices (VI) (Wang et al., 2021). NDVI is a widely used spectral index for assessing crop or vegetation health. Fig. 11 shows the NDVI trend of the flooded cropland before, during, and after the flood events. In 2020, the statistical average NDVI gradually increased from July to September and reached its peak with a value of 0.63 (healthy and thriving crop condition) on 16th September (Fig. 11a and v). This period corresponds to the early stage of flooding, before the water reached the central cropland region. However, the NDVI value dropped to 0.28 on 26th September (Fig. 11b and v), which is a day after the peak period of the flood and the time when the flood reached most of the cropland portion (Fig. 6e). The NDVI value further dropped to −0.17 (crops heavily submerged in flood water) on 1st October in 2020, which corresponds to the 49th day after the flood began and the 17th day after the flood reached the central cropland region (Section 3.4). The average NDVI values of the flooded cropland did not rise after the flood in 2020 until the 11th of October (0.25, partial flooding), and this value is very low compared to the NDVI before the flood (0.54) and in the years without floods (Fig. 11v).

A similar trend was observed in 2022. NDVI peaked on July 13, 2022 before the flood (Fig. 11h and v), but it gradually decreased as the flood commenced. A sharp drop can be observed in the average NDVI (−0.134, flooded crops with dominant flood water coverage) on September 26, 2022 (Fig. 11w and v). This date corresponds to the peak period of the flood and the 54th day after the 2022 flood began (Fig. 9).

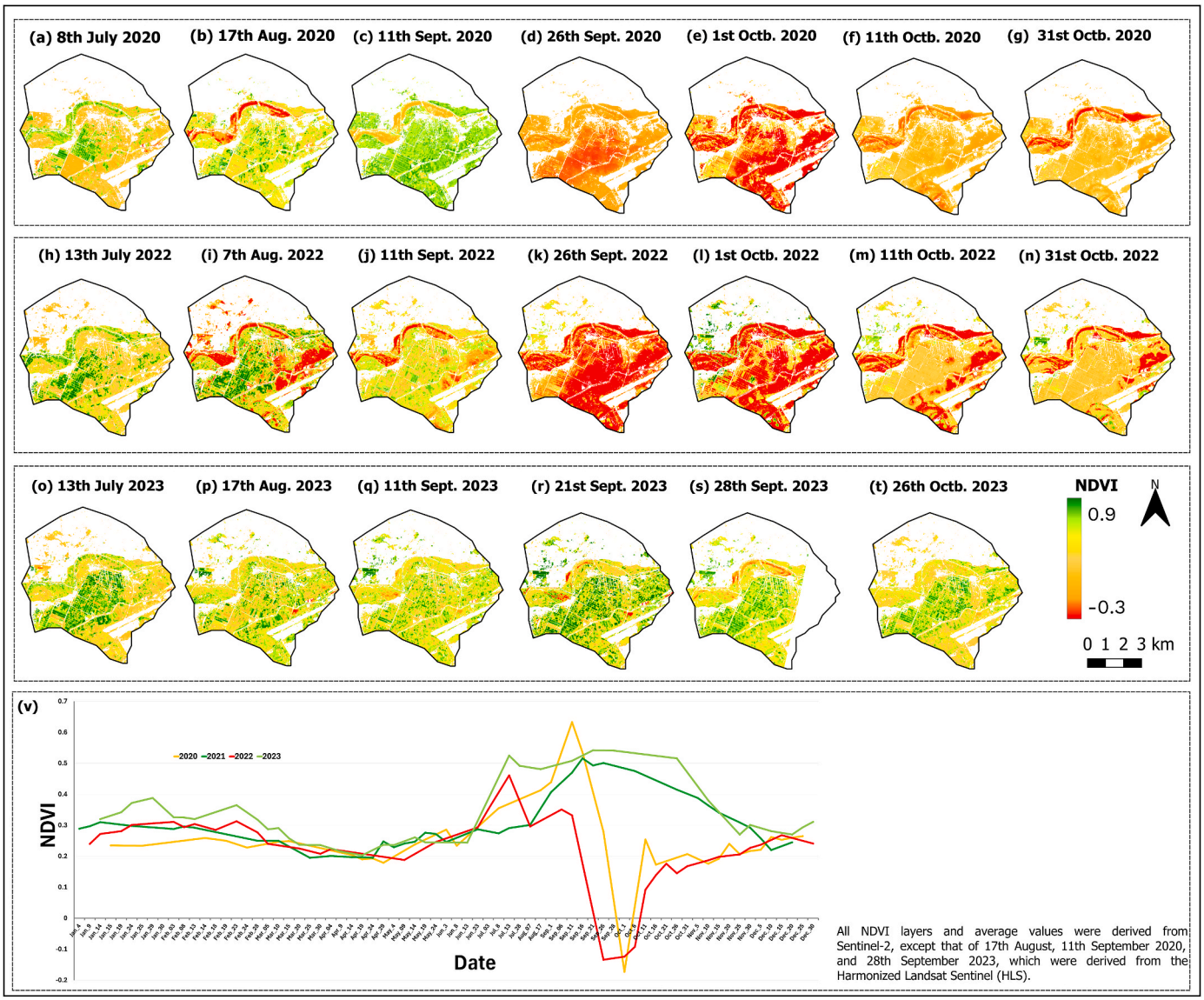

Fig. 11. NDVI dynamic flooded cropland before, during, and after the flood (a–g) in 2020, (h–n) in 2022, and (o–t) in the2023 - the year without flood, and (v) the average NDVI values of flooded cropland from January to December of 2020–2023.

The NDVI values of the flooded cropland did not rise until 11th of October (0.09, significant water presence). This value remained much lower than pre-flood levels (0.46) and the NDVI recorded during the same period in 2021 and 2023, when no flooding occurred.

Furthermore, post-flood NDVI values in both 2020 and 2022 remained consistently lower than those recorded in 2023, a non-flood year. The NDVI values only match those of 2023 on 25 November, approximately 62–67 days after most cropland was inundated. Since rainfed crops are planted in July and grow through August and September, the floods significantly impacted crop growth and maturity. The recovery of crops following the flood is depicted in Fig. 12.

As shown in Figs. 9 and 11, most cropland remained unaffected by flooding until September 25, 2020, and September 20, 2022. The S-2 images (Fig. 12a–c and 12f-h) indicate conditions before flooding on September 11, at the peak of flooding on September 20 and 26, and after flooding receded on October 11. Fig. 12c and h shows part of the training and testing samples used for crop recovery classification. The NDVI values of the "recovered" points in the post-flooding image are positive, higher than during the flooding, and closer to the pre-flooding values. For the "unrecovered (I)" points, their NDVI values fall between the pre-flooding and during-flooding values. The NDVI values of the "unrecovered (II)" points are negative and remain similar during and after the flooding (Fig. 12k and l). The full set of training and test points used for recovery classification is shown in Fig. S13.

In 2020, 2.83 km^2 (13 %) of the flooded cropland recovered, while in 2022, the recovered area was 3.96 km^2 (16 %). The remaining unrecovered part of the flooded cropland was 18.96 km^2 (87 %) and 21.38 km^2 (86 %) in 2020 and 2022, respectively (Fig. 11m). The spatial variation of the recovery pattern of the flooded cropland in 2020 and 2022 is depicted in Fig. 12e and j. The recovered cropland exhibits a similar pattern in both years, mainly in the southwest and the northern part of the study region. However, the recovery pattern in the central and southern parts varied between 2020 and 2022. In 2020, much of the central cropland remained inundated, due to the later onset of flooding compared to 2022, which affected the duration of water retention. In both years, most flooded cropland near the river, particularly in the central and eastern parts of the study area, did not recover after the flood.

197 (96 %) of farmers reported they suffered complete crop loss due to the flooding in 2022 (Section 2.2.5). When compared with the responses from the farmers during the participatory mapping, the results of the 2022 ML crop recovery classification confirmed that 179 (91 %) of

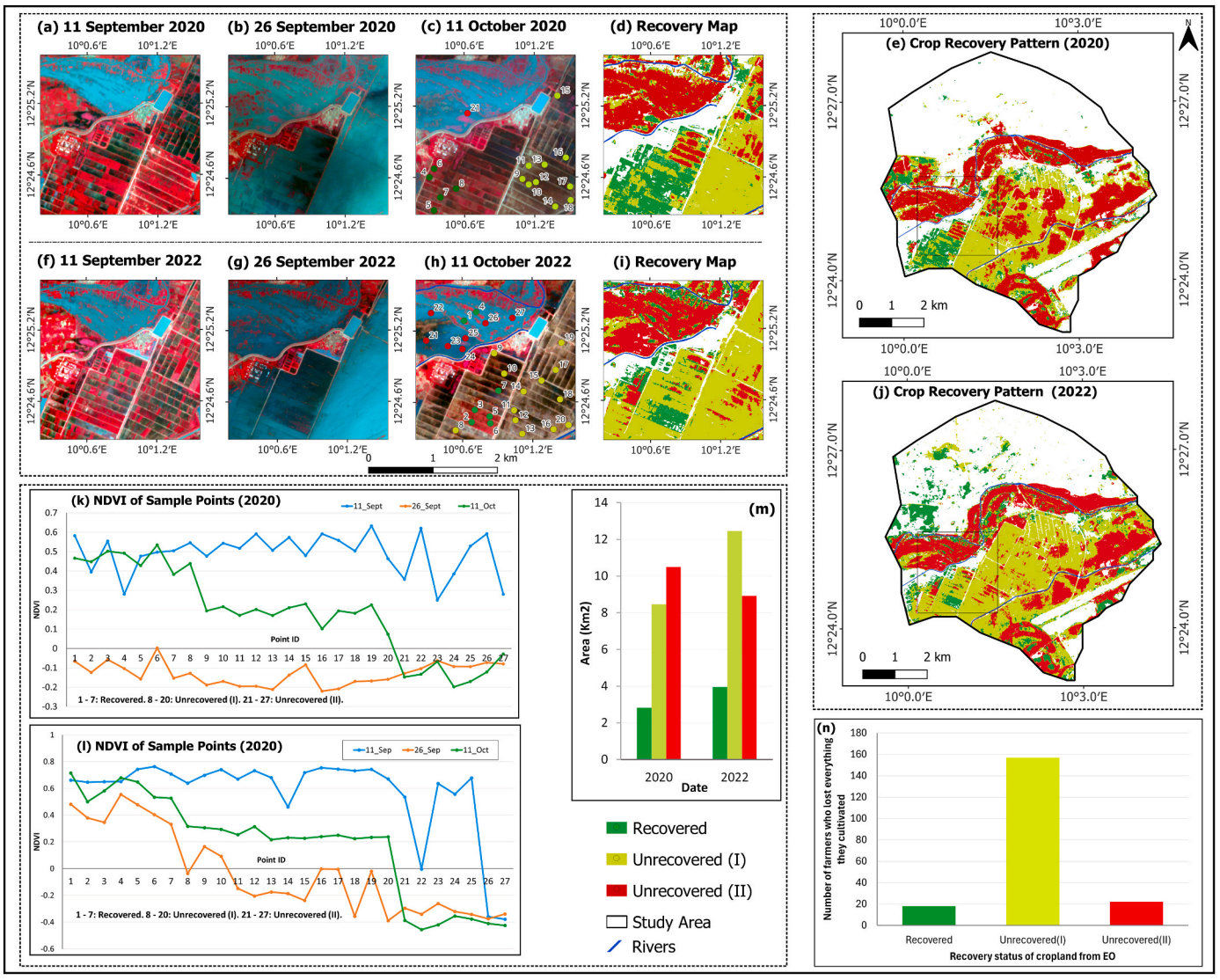

Fig. 12. Sentinel-2 FCC images (a & f) before the flooding reached most of the cropland, (b & g) during the peaks of the flooding, (c & h) post-flooding, (d & i) a portion of the crop recovery maps, (e & j) full extents of the crop recovery maps, (k & l) NDVI trend of sampled points used for crop recovery ML classification, (m) statistical area of recovered and unrecovered cropland, and (n) distribution of cropland recovery status from EO among farmers who experienced complete crop loss in 2022.

Table 8
Error matrix of the land cover map.

		Reference (Ground truth)								
		Bare soil	Built-up	Cultivated land	Fallow land	Tree	Water	Total	UA (%)	
Map (Predicted)	Bare soil	9	1	0	3	1	0	14	64.29	
	Built-up	2	25	0	0	1	0	28	89.29	
	Cultivated land	0	0	35	2	2	0	39	89.74	
	Fallow land	2	1	9	30	2	1	45	66.67	
	Tree	1	0	2	1	10	0	14	71.43	
	Water	0	0	0	0	0	20	20	100.00	
	Total	14	27	46	36	16	21	160		
	PA (%)	64.29	92.59	76.09	83.33	62.50	95.24		**OA**	**80.63 %**

farmers who reported total crop loss truly did not experience recovery (Fig. 12n). Conversely, 18 (9 %) of the cropland from the participatory mapping successfully recovered after the flooding. Among the 91 % of cropland classified as unrecovered based on Earth Observation (EO) data, 80 % fell into the "unrecovered I″ category, where green vegetation disappeared after the flood peak, but no flood water remained. The remaining 11 % were classified as "unrecovered II," indicating the continued presence of floodwater even after the peak (Fig. 12c, h, & 12n). The crops affected were maize, millet, rice, and sorghum. More so, EO-based machine learning classification showed that, among the cropland plots identified as unrecovered in the participatory mapping, 22 rectangular cropland plots (11 %) experienced moderate damage, while 162 rectangular cropland plots (80 %) suffered severe damage.

Table 9
Error matrix of the flood extent maps.

		Reference (MNDWI from S-2)				
		Not_Flooded	Flooded	Total	**UA (%)**	**2020**
Map (RF from PS and S-1)	Not_Flooded	130	17	147	88.44	
	Flooded	10	143	153	93.46	
	Total	140	160	300		
	PA (%)	92.86 %	89.38 %	**OA**	91.00 %	
		Not_Flooded	Flooded	Total	**UA (%)**	**2022**
	Not_Flooded	119	4	123	96.75	
	Flooded	14	163	177	92.09	
	Total	133	167	300		
	PA (%)	89.47	97.60	**OA**	94.00 %	

3.7. Accuracy assessments

The quality of the land cover map can be judged as good by considering the inherent quality errors from the image classification (De Luca et al., 2019). The confusion matrix (Table 8), generated using 160 random points (Fig. S5), shows the errors of omission and commissions for each land cover class and the overall accuracy for the land cover map. The model produced a satisfactory result of classifying all the land cover classes with a thematic overall accuracy (OA) of 80.63 %. The highest user accuracies (UAs) were observed for water (100 %), cultivated land (89.74 %), and built-up areas (89.29 %). However, the "fallow land" class had a lower UA (66.67 %), likely due to the misclassification of cultivated and fallow land segments, as the imagery was captured during the transition to the rainy season. Similarly, the low UA of the bare soil class (64.29 %) can be attributed to the similarities in its reflectance with the fallow land and built-up classes. The accuracy results of the flood maps for 2020 and 2022 are shown in Table 9. The OA of the 2020 recovery map was 96 %, while that of 2022 was 98 % (Table S4).

3.8. Other effects of flooding on farmers and adaptation strategies

The most critical damaging effect of flooding on the farmers was the loss of cultivated crops, culminating in huge financial loss. Also, many farmers reported that their houses were damaged, and they sought shelter in makeshift camps during the flooding. Only 12 % of the farmers acknowledged receiving compensation after the flooding event, which is mostly monetary. 88 % of the farmers did not receive compensation for their loss, and they mentioned a paucity of compensation, lack of awareness, and their non-availability among the reasons. 84 % of the farmers claimed that the compensation did not match the proportion of the damage that they suffered. Their adaptation measure is mainly a community (of farmers) collectively mounting embankments to prevent the flooding from reaching their farmland (Fig. S14).

4. Discussion

An improved framework for modelling crop damage and recovery due to flash floods was developed in this study. This advanced the methods of flooded crop damage and loss assessment, integrating time-series multi-sensor satellite imagery, participatory mapping, and high-resolution land cover data.

4.1. Flood causative factors

Understanding the cause of floods is important for flood extent mapping, mitigation plans and adopting the damage results. The floods in the study region, where this new framework was tested, were primarily rainfall-driven due to the heavy and continuous rainfall experienced in August and September of 2020 and 2022. The timing of flood onset and peak in both years closely followed the rainfall pattern (Figs. 3, 6 and 7). The series of continuous rainfall triggered the release of water from dams (Premium Times, 2022b) and caused an overflow of rivers, which culminated in floods, as mentioned by the farmers during the participatory mapping. This highlights the high vulnerability of the region to flooding during periods of torrential rainfall, as observed in previous studies by Tudunwada and Abbas (2022) and supports calls from climate experts for the permanent relocation of people in this area (Daily Nigerian, 2021). Furthermore, the region's topography plays a crucial role in the movement of accumulated rainfall water. The cropland in the central part of the study area is particularly susceptible, as it lies in a valley that traps runoff from surrounding areas (Figs. 8 and 9, & S15). Rainfall and slope were also identified as the major causes of flooding in the study region by Tudunwada and Abbas (2022).

4.2. Flood mapping and accuracy

The precision of flood extent is crucial for evaluating the damage and recovery of submerged crops. The flood maps for both years, with an overall accuracy exceeding 90 % (Table 9), provide a dependable basis for the flooded crop damage and recovery analyses. The high accuracy of the flood maps shows the importance of time series satellite images with high-temporal frequencies and the integration of optical and SAR images, which allows for a more precise capture of flood dynamics. The extent of the flood in this study region is changing rapidly with rainfall patterns, which would not be possible to precisely map with composite images. This approach represents a significant improvement over the monthly or weekly composites commonly used in previous studies. This aligns with the growing trend within the remote sensing community toward hybrid flood mapping approaches using SAR and optical satellite images for improved flood extent delineation (Sadiq et al., 2023) with proven case studies in (Cian et al., 2024; Ticehurst and Karim, 2023; Tong et al., 2018). The effectiveness of the Random Forest (RF) algorithm and supervised classification in accurately delineating flood extents is confirmed by this study. This finding is consistent with the findings of Zhang et al. (2021), where an object-based RF was applied to Sentinel-1 time-series data for flood mapping in a floodplain region of China, and Bayik et al. (2018), who also used RF for flood mapping in the agricultural landscape of the Meric River in northwest Turkey. The flood progression maps for 2020 and 2022 show that flooding initially impacted the northern and eastern regions, with the central croplands becoming inundated only during the peak flood period in September. However, flood dynamics varied between the two years. The satellite imagery demonstrates that the timing of the floods in both years corresponds closely with media reports. For the CDAT approach of flood extent mapping, the value of 1.5 as the coefficient (*fc*) used in Clement et al. (2018) & Long et al. (2014) was not suitable for this study region, and this supports the finding of C. Li et al. (2022a). Also, CDAT underestimated the flood extent due to significant variations in the backscatter coefficient distribution of single-date Sentinel-1 images during the flood events, as well as the monthly composite images used for flood extent mapping (Fig. S10 and S11).

4.3. Impacts of flood on cropland and degree of damage

A similar extent of cropland was flooded in both 2020 and 2022. The flooding affected an identical 20.56 km^2 of cropland in both years, accounting for 55 % of the total cropland area. This represents significant damage to the cropland, which is the major means of livelihood in the region. The participatory mapping result indicates that most farmers reported severe damage to their croplands due to the floods. The use of time-series satellite images allowed for the estimation of flood duration on cropland. Farmers whose cropland experienced short-term flooding, as little as 1 day, suffered severe crop damage, while those who also suffered severe damage had their farms submerged for as long as 86 days

(Fig. 10b and c). This variation in damage severity may be attributed to the intensity of the rainfall that contributed to the flood events.

4.4. Agreement between crop recovery status using EO and participatory mapping

The comparison between farmers' reported crop losses and the EO-based crop recovery classification yielded a high degree of consistency. Specifically, 96 % of farmers reported a complete loss of their crops in 2022 during the participatory mapping, and the EO-based recovery classification confirms that 91 % of these farmers did not observe any recovery in their cropland (Fig. 12n). This finding aligns with previous studies that reported consistency between estimated crop losses from geo-hydraulic modelling and those reported by farmers (Shrestha et al., 2021). Furthermore, it supports the notion that a high level of participation in mapping efforts produces statistically significant results (Steinke et al., 2017). Over both years, more than 85 % of cropland showed no recovery, predominantly cropland areas adjacent to the river in the central and eastern part of the study region. These regions correspond to areas with a prolonged duration of flooding in both years (Fig. S16). The crop recovery classification map revealed that most cropland plots that recovered were those where rice was cultivated. These recovered rice farms were flooded for 1–13 days (Fig. S17). This demonstrates the rice crop's ability to recover from short-duration floods. This finding is coherent with Bofana et al. (2022), who reported that rice and maize inundated for 12 days survived after the flood in selected agrarian districts of Sofala province in Mozambique. In contrast, the unrecovered millet farms were flooded for 29–37 days. Also, most of the unrecovered rice farms were flooded for 54 days. The variation in flood duration for unrecovered rice farms ranged from 1 to 86 days (Fig. S18). This variation could be attributed to the different growing stages and depth of the flood (Win et al., 2018), the influence of flood characteristics/scale, and the data used to estimate the flood durations and recovery (Shrestha et al., 2021).

The combination of supervised classification and participatory mapping used to evaluate the recovery status of flood-affected cropland overcomes the limitation of using just vegetation indices. While the NDVI-based approach to crop recovery after a hazard has shown effectiveness, it is limited by the determination of the NDVI threshold to categorize the degree of damage and recovery because of the annual variability of climatic conditions and phenological stages (Wang et al., 2021), In addition to the NDVI trend analysis, this study integrated supervised classification to mitigate these uncertainties and provided a more robust framework for crop damage, loss, and recovery assessments.

The use of time-series of optical and SAR images with a substantial amount of survey data from participatory mapping allowed for a more accurate quantification of crop damage and recovery. This addressed the challenge of limited satellite imagery availability and the lack of direct evidence to correlate with the level of damage, as identified by Cai et al. (2017). Furthermore, the level of information contained in the participatory mapping used in this study enriched the damage assessment, surpassing previous studies where the participants only identified the extent of the flood and its duration (C. Li et al., 2022a; Tamiru Haile et al., 2023). However, some farmers claimed a size/area of damaged cropland that was larger than the size they cultivated, and most of the farmers claimed that they lost the same amount of crop in 2020 and 2022, which could be because they could not recall the actual amount they lost in 2020. These issues further justify the approach used in this study, which combines time-series Earth Observation (EO) data and participatory mapping for a more comprehensive crop damage and loss assessment.

While the study provides reliable framework and insights into crop flooding and recovery, the limited availability of daily images for flood mapping restricted the ability to capture more extent of flooding over time. Also, a few portions of the cropland may be uncultivated at the time of the study, which was not accounted for in the recovery analysis. The use of cropping practices reported by farmers in participatory mapping for recovery status, instead of a plot-level crop-type map, limited the ability to assess damages at the crop level. Different crops exhibit varying levels of resistance to flooding, and without precise crop-type data, the assessment could not account for these differences. The lack of information on crop growing stage limited the depth of analysis, as crops at different growth stages respond differently to flood.

5. Conclusions

This study presents an improved method for modelling crop damage and recovery due to flash floods using time-series multi-sensor satellite imagery, participatory mapping, and high-resolution land cover data. The reliability of the integrated method developed in this research was proven with consistent results from EO damage and recovery results and the losses reported by farmers through participatory mapping. The integrated approach presents a reliable and reproducible method for crop damage and loss assessment, which advances scientific methodologies. Also, this method will support policymakers like UNDP and FAO in disaster response and agricultural resilience, addressing challenges with inconsistent flood impact data, especially as the UN launched a fund for climate-induced disaster relief. The second research objective was successfully achieved, with results showing over 90 % accuracy for the flood extent layers in 2020 and 2022. This demonstrates the effectiveness of supervised machine learning and combining optical and SAR time-series images from multiple sensors, offering a more accurate representation of flood extents and dynamics than either sensor alone. The use of free GEE cloud-computing and open-source QGIS software ensures the reproducibility of the methodology, paving the way for full automation in future flood damage assessments. The study's findings provide valuable insights on the impacts of floods on crop production and farmers' livelihood, which will assist policymakers in agriculture on post-disaster management plans and spatial planning to accommodate future cropland expansion in response to rapid population growth. Furthermore, the flood extent layers from this study contribute significantly to flood inventory databases, addressing data scarcity in the study region. The study highlights the severity of crop losses in the region and the inefficacy of current flood prevention measures employed by farmers. Future research should incorporate a plot-level crop-type map, crop growth stages, and flood depth variations to enhance the precision of flooded crop damage assessments.

CRediT authorship contribution statement

Lukumon Olaitan Lateef: Writing – review & editing, Writing – original draft, Visualization, Validation, Software, Methodology, Formal analysis, Data curation, Conceptualization. **Hugo Costa:** Writing – review & editing, Supervision, Methodology. **Pedro Cabral:** Writing – review & editing, Supervision, Methodology, Funding acquisition.

Code availability

The codes used for the analysis are available on this GitHub repository: https://github.com/Surv-Lukmon/Improved-Integrated-Framework-for-Flooded-Crop-Damage-and-Recovery-Assessment.

Declaration of generative AI and AI-assisted technologies in the writing process

During the preparation of this work, the authors used Generative AI to debug some codes. After using this tool/service, the authors reviewed and edited the content as needed and take full responsibility for the content of the published article.

Funding

The acquisition of the rainfall data used in this data was funded by NOVA Information Management School (NOVA-IMS) of Universiade NOVA de Lisboa under the Erasmus-Mundus Geospatial Technologies Programme.

Declaration of competing interest

The authors declare that they have no known competing financial interests or personal relationships that could have appeared to influence the work reported in this paper.

Acknowledgments

This work was partially supported by national funds through FCT (Fundação para a Ciência e a Tecnologia) under the project - UIDB/04152/2020 (DOI: 10.54499/UIDB/04152/2020) - Centro de Investigação em Gestão de Informação (MagIC)/NOVA IMS). We acknowledge NOVA Information Management School (NOVA IMS), Universidade NOVA de Lisboa for covering the open-access charge for this publication. The authors appreciate Professor Filiberto Pla Bañón and Professor Marco Painho for their feedback on the research idea conceptualization and analyses that helped improve the quality of this work. Salma Nuhu, Saifuddeen Lawan Madachi, and Aliyu Nuhu Abdullahi are also appreciated for their assistance in collecting data through participatory mapping. We also thank the anonymous reviewers for their helpful comments which improved the manuscript.

Appendix A. Supplementary data

Supplementary data to this article can be found online at https://doi.org/10.1016/j.jenvman.2025.125542.

Data availability statement

The data sources are listed in Table 1. The Sentinel 1/2 images are freely available and accessible on the Copernicus website or via the GEE computing platform/data catalog. The PlanetScope images used in this study were accessed using an educational/research account. The participatory mapping data is available upon request from the corresponding author. The other datasets used and generated in this research are available in Zenodo repository: https://doi.org/10.5281/zenodo.15204588 (Lateef et al., 2025).

References

Amaechina, E.C., Anugwa, I.Q., Agwu, A.E., Ifelunini, A.I., Umeonuora, T.G., Okwor, C. A., 2022. Assessing climate change-related losses and damages and adaptation constraints to address them: evidence from flood-prone riverine communities in Southern Nigeria. Environ. Dev. 44, 100780. https://doi.org/10.1016/j.envdev.2022.100780.

Associated Press, 2022. West Africa Floods Destroy Crops, Worsening Hunger Fears.

Bayik, C., Abdikan, S., Ozbulak, G., Alasag, T., Aydemir, S., Balik Sanli, F., 2018. Exploiting multi-temporal SENTINEL-1 SAR data for flood extend mapping. Int. Arch. Photogram. Rem. Sens. Spatial Inf. Sci. XLII-3/W4, 109–113. https://doi.org/10.5194/isprs-archives-XLII-3-W4-109-2018.

Bofana, J., Zhang, M., Wu, B., Zeng, H., Nabil, M., Zhang, N., Elnashar, A., Tian, F., Da Silva, J.M., Botão, A., Atumane, A., Mushore, T.D., Yan, N., 2022. How long did crops survive from floods caused by Cyclone Idai in Mozambique detected with multi-satellite data. Remote Sens. Environ. 269, 112808. https://doi.org/10.1016/j.rse.2021.112808.

Brémond, P., Grelot, F., Agenais, A.-L., 2013. Review Article: economic evaluation of flood damage to agriculture – review and analysis of existing methods. Nat. Hazards Earth Syst. Sci. 13, 2493–2512. https://doi.org/10.5194/nhess-13-2493-2013.

Brigham, C., Gilbert, S., Xu, Q., 2011. Open Geospatial Data: an Assessment of Global Boundary Datasets.

Bush, J., 2012. Hadejia Valley MIXED ECONOMY.

Cai, X., Haile, A.T., Magidi, J., Mapedza, E., Nhamo, L., 2017. Living with floods – household perception and satellite observations in the Barotse floodplain, Zambia. Phys. Chem. Earth, Parts A/B/C 100, 278–286. https://doi.org/10.1016/j.pce.2016.10.011.

Chen, Z., Zhao, S., 2022. Automatic monitoring of surface water dynamics using Sentinel-1 and Sentinel-2 data with Google Earth Engine. Int. J. Appl. Earth Obs. Geoinformation 113, 103010. https://doi.org/10.1016/j.jag.2022.103010.

Chen, H., Liang, Q., Liang, Z., Liu, Y., Xie, S., 2019. Remote-sensing disturbance detection index to identify spatio-temporal varying flood impact on crop production. Agric. For. Meteorol. 269–270, 180–191. https://doi.org/10.1016/j.agrformet.2019.02.002.

Chiaka, J.C., Zhen, L., Yunfeng, H., Xiao, Y., Muhirwa, F., Lang, T., 2022. Smallholder farmers contribution to food production in Nigeria. Front. Nutr. 9, 916678. https://doi.org/10.3389/fnut.2022.916678.

Cian, F., Marconcini, M., Ceccato, P., 2018. Normalized Difference Flood Index for rapid flood mapping: taking advantage of EO big data. Remote Sens. Environ. 209, 712–730. https://doi.org/10.1016/j.rse.2018.03.006.

Cian, F., Delgado Blasco, J.M., Ivanescu, C., 2024. Improving rapid flood impact assessment: an enhanced multi-sensor approach including a new flood mapping method based on Sentinel-2 data. J. Environ. Manag. 369, 122326. https://doi.org/10.1016/j.jenvman.2024.122326.

Clement, M.A., Kilsby, C.G., Moore, P., 2018. Multi-temporal synthetic aperture radar flood mapping using change detection. J. Flood Risk Manag. 11, 152–168. https://doi.org/10.1111/jfr3.12303.

Cui, J., Guo, Y., Xu, Q., Li, D., Chen, W., Shi, L., Ji, G., Li, L., 2023. Extraction of information on the flooding extent of agricultural land in henan province based on multi-source remote sensing images and Google Earth engine. Agronomy 13, 355. https://doi.org/10.3390/agronomy13020355.

Daily Nigerian, 2021. UN Climate Expert Issues Red Alert, Advises Relocation of Hadejia Town over Impending Floods.

Daily Post, 2020. Flood Displaces 10,000 Persons, Destroys 100,000 Hectares of Farmlands in Jigawa.

Daily Trust, 2020. Flood Kills 40 in Jigawa.

De Luca, G., Silva, J.M.N., Cerasoli, S., Araújo, J., Campos, J., Di Fazio, S., Modica, G., 2019. Object-based land cover classification of cork oak woodlands using UAV imagery and Orfeo ToolBox. Remote Sens. 11, 1238. https://doi.org/10.3390/rs11101238.

Demissie, B., Vanhuysse, S., Grippa, T., Flasse, C., Wolff, E., 2023. Using Sentinel-1 and Google Earth Engine cloud computing for detecting historical flood hazards in tropical urban regions: a case of Dar es Salaam. Geomat. Nat. Hazards Risk 14, 2202296. https://doi.org/10.1080/19475705.2023.2202296.

DMI Jigawa State, D.M.I. DMI J.S., 2022. The people affected by floods are in dire need of shelter at the moment. URL. https://www.facebook.com/101390434870179/posts/pfbid0vsPbcEFCu1sMbKjsLCrXP6eeSnTiXrUDvFi5wkrKqGFhicdEaXyGxwgCkm7TxJx9l/?app=fbl. accessed 9.20.23.

Dodangeh, P., Shah-Hosseini, R., 2023. Extraction of flood-affected agricultural lands in the google earth engine; case study of Khuzestan, Iran. ISPRS Ann. Photogramm. Remote Sens. Spat. Inf. Sci. 123–128. https://doi.org/10.5194/isprs-annals-X-4-W1-2022-123-2023. X-4/W1-2022.

Echendu, A.J., 2022. Flooding, food security and the sustainable development goals in Nigeria: an assemblage and systems thinking approach. Soc. Sci. 11, 59. https://doi.org/10.3390/socsci11020059.

European Space Agency (ESA),n.d. SENTINEL-2 MISSION GUIDE. Sentin.-2 MISSION GUIDE. URL https://sentinels.copernicus.eu/web/sentinel/missions/sentinel-2 (accessed 1.31.24a).

European Space Agency (ESA), n.d. Sentinel-1.

European Space Agency, Airbus, 2022. Copernicus DEM. https://doi.org/10.5270/ESA-c5d3d65.

Floodlist, 2022. Nigeria – Deadly Floods in Jigawa State.

Food and Agriculture Organization (FAO), 2015. Global Administrative Unit Layers (GAUL).

Food and Agriculture Organization (FAO), 2023a. The Impact of Disasters on Agriculture and Food Security 2023. FAO, Rome. https://doi.org/10.4060/cc7900en.

Food and Agriculture Organization (FAO), 2023b. Northeastern Nigeria: Humanitarian Response Plan 2023. FAO, Rome. https://doi.org/10.4060/cc5192en.

Food and Agriculture Organization (FAO), 2023c. Nigeria - crop calendar. URL. https://data-in-emergencies.fao.org/documents/bc77ee36347a46549f927cf7bb3e5501/about. accessed 8.19.23.

Gorelick, N., Hancher, M., Dixon, M., Ilyushchenko, S., Thau, D., Moore, R., 2017. Google Earth engine: planetary-scale geospatial analysis for everyone. Remote Sens. Environ. 202, 18–27. https://doi.org/10.1016/j.rse.2017.06.031.

History Hub, 2020. This is Hadeja, Jigawa state Nigeria. URL. https://www.facebook.com/story.php/?id=100063674667241&story_fbid=400585878009714&paipv=0&eav=AfZx07lzJvlycYzXzB5TXR7CewGKA7JoUsgDuyDrYMDRRRPuUmsQ_o9cTK57op9k9Po&_rdr. (Accessed 8 December 2023).

Idoko, I., 2016. An impact assessment of flooding on food security among rural farmers in dagiri community, of Gwagwalada area council, Abuja, Nigeria. Agric. Dev. (Montpellier) 1, 6–13. https://doi.org/10.20448/journal.523/2016.1.1/523.1.6.13.

Intergovernmental Panel on Climate Change (IPCC), 2023. Climate Change 2022 – Impacts, Adaptation and Vulnerability: Working Group II Contribution to the Sixth Assessment Report of the Intergovernmental Panel on Climate Change, first ed. Cambridge University Press. https://doi.org/10.1017/9781009325844.

Jamali, A., Roy, S.K., Hashemi Beni, L., Pradhan, B., Li, J., Ghamisi, P., 2024. Residual wave vision U-Net for flood mapping using dual polarization Sentinel-1 SAR imagery. Int. J. Appl. Earth Obs. Geoinformation 127, 103662. https://doi.org/10.1016/j.jag.2024.103662.

Jigawa State Government, 2017. Peoples and culture. URL. https://jigawastate.gov.ng/people_culture.php. accessed 8.19.23.

Kang, J., Yang, X., Wang, Z., Huang, C., Wang, J., 2022. Collaborative extraction of paddy planting areas with multi-source information based on Google Earth Engine: a

case study of Cambodia. Remote Sens 14 (8), 1823. https://doi.org/10.3390/rs14081823.
Kumar, H., Karwariya, S.K., Kumar, R., 2022. Google Earth engine-based identification of flood extent and flood-affected paddy rice fields using sentinel-2 MSI and Sentinel-1 SAR data in Bihar state, India. J. Indian Soc. Remote Sens. 50, 791–803. https://doi.org/10.1007/s12524-021-01487-3.
Lateef, L.O., Costa, H., Cabral, P., 2025. HAD-FCDR25: multi-source flood, crop damage, and recovery dataset for Hadejia, Nigeria. https://doi.org/10.5281/zenodo.15204588.
Li, C., Dash, J., Asamoah, M., Sheffield, J., Dzodzomenyo, M., Gebrechorkos, S.H., Anghileri, D., Wright, J., 2022a. Increased flooded area and exposure in the White Volta river basin in Western Africa, identified from multi-source remote sensing data. Sci. Rep. 12, 3701. https://doi.org/10.1038/s41598-022-07720-4.
Li, M., Zhang, T., Tu, Y., Ren, Z., Xu, B., 2022b. Monitoring post-flood recovery of croplands using the integrated Sentinel-1/2 imagery in the Yangtze-Huai river basin. Remote Sens. 14, 690. https://doi.org/10.3390/rs14030690.
Long, S., Fatoyinbo, T.E., Policelli, F., 2014. Flood extent mapping for Namibia using change detection and thresholding with SAR. Environ. Res. Lett. 9, 035002. https://doi.org/10.1088/1748-9326/9/3/035002.
Manjusree, P., Prasanna Kumar, L., Bhatt, C.M., Rao, G.S., Bhanumurthy, V., 2012. Optimization of threshold ranges for rapid flood inundation mapping by evaluating backscatter profiles of high incidence angle SAR images. Int. J. Disaster Risk Sci. 3, 113–122. https://doi.org/10.1007/s13753-012-0011-5.
Martinis, S., Twele, A., Voigt, S., 2009. Towards operational near real-time flood detection using a split-based automatic thresholding procedure on high resolution TerraSAR-X data. Nat. Hazards Earth Syst. Sci. 9, 303–314. https://doi.org/10.5194/nhess-9-303-2009.
Matgen, P., Hostache, R., Schumann, G., Pfister, L., Hoffmann, L., Savenije, H.H.G., 2011. Towards an automated SAR-based flood monitoring system: lessons learned from two case studies. Phys. Chem. Earth, Parts A/B/C 36, 241–252. https://doi.org/10.1016/j.pce.2010.12.009.
Maxwell, A.E., Warner, T.A., Fang, F., 2018. Implementation of machine-learning classification in remote sensing: an applied review. Int. J. Rem. Sens. 39, 2784–2817. https://doi.org/10.1080/01431161.2018.1433343.
Miao, S., Zhao, Y., Huang, J., Li, X., Wu, R., Su, W., Zeng, Y., Guan, H., Abd Elbasit, M.A. M., Zhang, J., 2023. A comprehensive evaluation of flooding's effect on crops using satellite time series data. Remote Sens. 15, 1305. https://doi.org/10.3390/rs15051305.
Michael, P.S., Sanga, H.G., Shitindi, M.J., Herzog, M., Meliyo, J.L., Massawe, B.H.J., 2023. Uncovering spatiotemporal pattern of floods with Sentinel-1 synthetic aperture radar in major rice-growing river basins of Tanzania. Front. Earth Sci. 11, 1183834. https://doi.org/10.3389/feart.2023.1183834.
Monteleone, B., Giusti, R., Magnini, A., Arosio, M., Domeneghetti, A., Borzì, I., Petruccelli, N., Castellarin, A., Bonaccorso, B., Martina, M.L.V., 2023. Estimations of crop losses due to flood using multiple sources of information and models: the case study of the panaro river. Water 15, 1980. https://doi.org/10.3390/w15111980.
National Aeronautics and Space Administration (NASA), 2023. Harmonized Landsat and Sentinel-2 (HLS).
National Emergency Management Agency (NEMA), 2023. URL. https://twitter.com/nemanigeria/status/1617603180296273920. accessed 5.13.23.
Nigeria Hydrological Services Agency, 2022. 2022 Annual Flood Outlook Publication.
Nigerian Meteorological Agency (NiMet), 2023. Daily Rainfall and Precipitation Data for Jigawa, 2012 - 2023).
Otsu, N., 1979. A threshold selection method from gray-level histograms. IEEE Trans. Syst. Man Cybern. 9, 62–66. https://doi.org/10.1109/TSMC.1979.4310076.
Pandey, A.C., Kaushik, K., Parida, B.R., 2022. Google Earth engine for large-scale flood mapping using SAR data and impact assessment on agriculture and population of Ganga-Brahmaputra basin. Sustainability 14, 4210. https://doi.org/10.3390/su14074210.
Pantaleoni, E., Engel, B.A., Johannsen, C.J., 2007. Identifying agricultural flood damage using Landsat imagery. Precis. Agric. 8, 27–36. https://doi.org/10.1007/s11119-006-9026-5.
Planet Labs, 2023a. PlanetScope. URL. https://developers.planet.com/docs/data/planetscope/. accessed 1.18.24.
Planet Labs, 2023b. Understanding PlanetScope instruments. URL. https://developers.planet.com/docs/apis/data/sensors/. accessed 11.11.23.
Premium Times, 2022a. SPECIAL REPORT: Floods Devastate Farmlands, Raise Fear of Food Insecurity in Nigeria.
Premium Times, 2022b. Flood: Jigawa Farmers Demand Compensation from Hadejia-Jamare River Basin Authority.
Qamer, F.M., Abbas, S., Ahmad, B., Hussain, A., Salman, A., Muhammad, S., Nawaz, M., Shrestha, S., Iqbal, B., Thapa, S., 2023. A framework for multi-sensor satellite data to evaluate crop production losses: the case study of 2022 Pakistan floods. Sci. Rep. 13, 4240. https://doi.org/10.1038/s41598-023-30347-y.
Rahman, M.S., Di, L., 2020. A systematic review on case studies of remote-sensing-based flood crop loss assessment. Agriculture 10, 131. https://doi.org/10.3390/agriculture10040131.
Reed, C., Anderson, W., Kruczkiewicz, A., Nakamura, J., Gallo, D., Seager, R., McDermid, S.S., 2022. The impact of flooding on food security across Africa. Proc. Natl. Acad. Sci. 119, e2119399119. https://doi.org/10.1073/pnas.2119399119.
Roy, D.P., Huang, H., Houborg, R., Martins, V.S., 2021. A global analysis of the temporal availability of PlanetScope high spatial resolution multi-spectral imagery. Remote Sens. Environ. 264, 112586. https://doi.org/10.1016/j.rse.2021.112586.
Sadiq, R., Imran, M., Ofli, F., 2023. Remote sensing for flood mapping and monitoring. In: Singh, A. (Ed.), International Handbook of Disaster Research. Springer Nature Singapore, Singapore, pp. 679–697. https://doi.org/10.1007/978-981-19-8388-7_178.
Saleh, T., Holail, S., Xiao, X., Xia, G.-S., 2024. High-precision flood detection and mapping via multi-temporal SAR change analysis with semantic token-based transformer. Int. J. Appl. Earth Obs. Geoinformation 131, 103991. https://doi.org/10.1016/j.jag.2024.103991.
Shrestha, B.B., Kawasaki, A., Zin, W.W., 2021. Development of flood damage functions for agricultural crops and their applicability in regions of Asia. J. Hydrol. Reg. Stud. 36, 100872. https://doi.org/10.1016/j.ejrh.2021.100872.
Singha, M., Dong, J., Sarmah, S., You, N., Zhou, Y., Zhang, G., Doughty, R., Xiao, X., 2020. Identifying floods and flood-affected paddy rice fields in Bangladesh based on Sentinel-1 imagery and Google Earth Engine. ISPRS J. Photogrammetry Remote Sens. 166, 278–293. https://doi.org/10.1016/j.isprsjprs.2020.06.011.
Steinke, J., Van Etten, J., Zelan, P.M., 2017. The accuracy of farmer-generated data in an agricultural citizen science methodology. Agron. Sustain. Dev. 37, 32. https://doi.org/10.1007/s13593-017-0441-y.
Tamiru Haile, A., Worku Bekele, T., Rientjes, T., 2023. Interannual comparison of historical floods through flood detection using multi-temporal Sentinel-1 SAR images, Awash River Basin, Ethiopia. Int. J. Appl. Earth Obs. Geoinformation 124, 103505. https://doi.org/10.1016/j.jag.2023.103505.
The Cable, 2022. UNDER WATER: Jigawa Farmers Face Season of Pain as Flood Robs Them of Harvest.
Thenkabail, Prasad S., Teluguntla, Pardhasaradhi G., Xiong, Jun, Oliphant, Adam, Congalton, Russell G., Ozdogan, Mutlu, Krishna Gumma, Murali, Tilton, James C., Giri, Chandra, Milesi, Cristina, Phalke, Aparna, Massey, Richard, Yadav, Kamini, Sankey, Temuulen, Zhong, Ying, Aneece, Itiya, Foley, Daniel, 2021. Global Cropland-Extent Product at 30-m Resolution (GCEP30) Derived from Landsat Satellite Time-Series Data for the Year 2015 Using Multiple Machine-Learning Algorithms on Google Earth Engine Cloud. U.S. Geological Survey, Reston, VA (Professional Paper), Professional Paper.
Thomas, V., López, R., 2015. Global increase in climate-related disasters. SSRN Electron. J. https://doi.org/10.2139/ssrn.2709331.
Ticehurst, C., Karim, F., 2023. Towards developing comparable optical and SAR remote sensing inundation mapping with hydrodynamic modelling. Int. J. Rem. Sens. 44, 2912–2935. https://doi.org/10.1080/01431161.2023.2211714.
Tong, X., Luo, X., Liu, Shuguang, Xie, H., Chao, W., Liu, Shuang, Liu, Shijie, Makhinov, A. N., Makhinova, A.F., Jiang, Y., 2018. An approach for flood monitoring by the combined use of Landsat 8 optical imagery and COSMO-SkyMed radar imagery. ISPRS J. Photogrammetry Remote Sens. 136, 144–153. https://doi.org/10.1016/j.isprsjprs.2017.11.006.
Torres, R., Snoeij, P., Geudtner, D., Bibby, D., Davidson, M., Attema, E., Potin, P., Rommen, B., Floury, N., Brown, M., Traver, I.N., Deghaye, P., Duesmann, B., Rosich, B., Miranda, N., Bruno, C., L'Abbate, M., Croci, R., Pietropaolo, A., Huchler, M., Rostan, F., 2012. GMES Sentinel-1 mission. Remote Sens. Environ. 120, 9–24. https://doi.org/10.1016/j.rse.2011.05.028.
Tudunwada, I.Y., Abbas, A., 2022. Flood vulnerability mapping and prediction for early warning in Jigawa State, Northern Nigeria, using geospatial techniques. Int. J. Disaster Risk Reduct. 79, 103156. https://doi.org/10.1016/j.ijdrr.2022.103156.
Umar, N., Gray, A., 2023. Flooding in Nigeria: a review of its occurrence and impacts and approaches to modelling flood data. Int. J. Environ. Stud. 80, 540–561. https://doi.org/10.1080/00207233.2022.2081471.
United Nations Development Programme (UNDP), 2023. Nigeria Flood Impact, Recovery and Mitigation Assessment Report 2022-2023.
United Nations Development Programme (UNDP), 2024. Loss and damage fund for developing countries. URL. https://www.undp.org/belarus/stories/loss-and-damage-fund-developing-countries. accessed 9.20.24.
United Nations Office for the Coordination of Humanitarian Affairs (OCHA), 2022. Nigeria - Floods Response: Flash Update 4 (Last Updated: 14 December 2022).
Waldner, F., De Abelleyra, D., Verón, S.R., Zhang, M., Wu, B., Plotnikov, D., Bartalev, S., Lavreniuk, M., Skakun, S., Kussul, N., Le Maire, G., Dupuy, S., Jarvis, I., Defourny, P., 2016. Towards a set of agrosystem-specific cropland mapping methods to address the global cropland diversity. Int. J. Rem. Sens. 37, 3196–3231. https://doi.org/10.1080/01431161.2016.1194545.
Wang, S., Chen, J., Rao, Y., Liu, L., Wang, W., Dong, Q., 2020. Response of winter wheat to spring frost from a remote sensing perspective: damage estimation and influential factors. ISPRS J. Photogrammetry Remote Sens. 168, 221–235. https://doi.org/10.1016/j.isprsjprs.2020.08.014.
Wang, S., Rao, Y., Chen, J., Liu, L., Wang, W., 2021. Adopting "difference-in-differences" method to monitor crop response to agrometeorological hazards with satellite data: a case study of dry-hot wind. Remote Sens. 13, 482. https://doi.org/10.3390/rs13030482.
Wang, L.-C., Hoang, D.V., Liou, Y.-A., 2022a. Quantifying the impacts of the 2020 flood on crop production and food security in the middle reaches of the Yangtze river, China. Remote Sens. 14, 3140. https://doi.org/10.3390/rs14133140.
Wang, X., Liu, Z., Chen, H., 2022b. Investigating flood impact on crop production under a comprehensive and spatially explicit risk evaluation framework. Agriculture 12, 484. https://doi.org/10.3390/agriculture12040484.
Win, S., Zin, W.W., Kawasaki, A., San, Z.M.L.T., 2018. Establishment of flood damage function models: a case study in the Bago River Basin, Myanmar. Int. J. Disaster Risk Reduct. 28, 688–700. https://doi.org/10.1016/j.ijdrr.2018.01.030.
Xu, H., 2006. Modification of normalised difference water index (NDWI) to enhance open water features in remotely sensed imagery. Int. J. Rem. Sens. 27, 3025–3033. https://doi.org/10.1080/01431160600589179.
Zhang, X., Chan, N.W., Pan, B., Ge, X., Yang, H., 2021. Mapping flood by the object-based method using backscattering coefficient and interference coherence of Sentinel-1

time series. Sci. Total Environ. 794, 148388. https://doi.org/10.1016/j.scitotenv.2021.148388.
Zhao, B., Sui, H., Liu, J., 2023. Siam-DWENet: flood inundation detection for SAR imagery using a cross-task transfer siamese network. Int. J. Appl. Earth Obs. Geoinformation 116, 103132. https://doi.org/10.1016/j.jag.2022.103132.
Zhou, W., Chen, F., Meng, Y., Chandrasekaran, U., Luo, X., Yang, W., Shu, K., 2020. Plant waterlogging/flooding stress responses: from seed germination to maturation. Plant Physiol. Biochem. 148, 228–236. https://doi.org/10.1016/j.plaphy.2020.01.020.